9-9-2010

Experimental simulation of Lunar Magma Ocean crystallization : insights into mantle composition and the source regions of lunar basaltic magmatism

Stephen Matthew Elardo

Recommended Citation

Elardo, Stephen Matthew. "Experimental simulation of Lunar Magma Ocean crystallization : insights into mantle composition and the source regions of lunar basaltic magmatism." (2010). https://digitalrepository.unm.edu/eps_etds/24

Stephen Matthew Elardo
Candidate

Earth and Planetary Sciences
Department

This thesis is approved, and it is acceptable in quality and form for publication:

Approved by the Thesis Committee:

C K, Chairperson

Carl B. Agee

EXPERIMENTAL SIMULATION OF LUNAR MAGMA OCEAN CRYSTALLIZATION: INSIGHTS INTO MANTLE COMPOSITION AND THE SOURCE REGIONS OF LUNAR BASALTIC MAGMATISM

BY

STEPHEN MATTHEW ELARDO

B.S., GEOLOGY/ EARTH AND SPACE SCIENCES
STONY BROOK UNIVERSITY, 2008

THESIS

Submitted in Partial Fulfillment of the
Requirements for the Degree of

Master of Science
Earth and Planetary Sciences

The University of New Mexico
Albuquerque, New Mexico

August, 2010

DEDICATION

To mom and dad, for never telling me that I couldn’t, or that I shouldn’t…

AKNOWLEDGEMENTS

First, I'd like to thank Dr. Dave Draper for not only taking a chance by bringing me to the IOM to work on this project and for the endless, patient support, but also for letting me take charge of the project and steer it in the directions I thought were best. I barely knew a thing about the Moon before coming to UNM, and if it weren't for Dr. Draper's willingness to turn the reins over to me early on, I don't think I would have grown as a scientist nearly as much as I have.

Next, I'd like to thank Dr. Chip Shearer for going above and beyond as a second advisor. Having him here to review my work, talk about ideas with and to keep me on track was nothing short of invaluable.

Lastly, I'd like to thank a number of scientists whose discussions with me at conferences, in the lab or elsewhere either helped focus or expand my thinking about lunar petrology, the LMO or experimental design, and thus contributed to this project. These people are, in no particular order, Dr.'s John Longhi, Jim Papike, Lindy Elkins-Tanton, Francis McCubbin, Penny King, Carl Agee, Adrian Brearley and Clive Neal. The insights they provided may have been small and in passing, but they helped shape my thoughts on the Moon and are therefore much appreciated. I'd also like to thank Loan Le at NASA Johnson Space Center for help with preparation of starting materials and Paul Burger for help with SIMS analyses.

EXPERIMENTAL SIMULATION OF LUNAR MAGMA OCEAN CRYSTALLIZATION: INSIGHTS INTO MANTLE COMPOSITION AND THE SOURCE REGIONS LUNAR BASALTIC MAGMATISM

BY

STEPHEN MATTHEW ELARDO

B.S., GEOLOGY/ EARTH AND SPACE SCIENCES
STONY BROOK UNIVERSITY, 2008

ABSTRACT OF THESIS

Submitted in Partial Fulfillment of the
Requirements for the Degree of

Master of Science
Earth and Planetary Sciences

The University of New Mexico
Albuquerque, New Mexico

August, 2010

Experimental Simulation of Lunar Magma Ocean Crystallization: Insights into Mantle Composition and the Source Regions of Lunar Basaltic Magmatism

By

Stephen Matthew Elardo

B.S., Geology/Earth and Space Sciences
Stony Brook University, 2008

ABSTRACT

Crystallization of the Lunar Magma Ocean has been empirically modeled and its products inferred from sample observations, but it has never been fully tested experimentally. Presented in this study is the first experimental simulation of lunar differentiation. Two end-member bulk Moon compositions are considered: one enriched in refractory lithophile elements relative to Earth and one with no such enrichment. A "two-stage" model of magma ocean crystallization based on geophysical models is simulated and features early crystal suspension and equilibrium crystallization followed by fractional crystallization of the residual liquid. An initially entirely molten Moon is assumed. The study presented below focuses on the early cumulates formed by equilibrium crystallization, differences in mantle mineralogy resulting from different bulk Moon compositions and the implications for the source regions for secondary lunar magmatism.

There are significant differences in the crystallization sequence between the two bulk compositions. Refractory element enriched bulk Moon compositions produce a deep mantle that contains garnet and minor Cr-spinel in addition to low-Ca pyroxene and olivine. Compositions without refractory element enrichment produce low-Ca pyroxene bearing dunite mantles without an aluminous phase such as garnet. The differences in bulk composition are magnified in the residual melt and the TWM residual will produce plagioclase and ilmenite earlier and in greater quantities. Both compositions produce Mg-rich early cumulate piles that extend from the core-mantle boundary to ~355 km depth, if 50% equilibrium crystallization and whole Moon melting are assumed. Although they physically encompass the depth of the low-Ti green glass source, mantle lithologies such as these provide poor fits for the green glass source regions. They are both too Mg-rich and Al- and Ca-poor. Thus, additional processes such as cumulate mixing must be called upon to create the green glass source at the appropriate depths. However, these early LMO cumulates provide good fits for the source regions for a component of the high-Mg*, Ni- and Co-poor parental magmas of the Mg-suite cumulates. These LMO cumulates could generate partial melts meeting the criteria of the Mg-suite parent by KREEP hybridization induced melting in the source and/or decompression melting followed by assimilation of a high-Al component.

TABLE OF CONTENTS

BACKGROUND

The Master of Science thesis below is a non-traditional thesis that has been written in the style of a peer-reviewed journal article. It will be submitted to a scientific journal as a standalone contribution in much the same form as it is presented here. The paper and thesis detail an experimental program designed to simulate crystallization of the Lunar Magma Ocean (LMO) and relate the results to both sample observations and empirical models of lunar differentiation. The following presents background information on the history of the LMO hypothesis, past and current models, outstanding problems, and the goals of this work.

The LMO hypothesis originally arose from examination of samples returned from the Apollo 11 mission in 1969. The pre-Apollo view of the Moon, however, grew out of centuries of telescopic observations and conjecture. Three theories dealing with lunar formation were most prominent and were (1) accretion alongside Earth as a double system, (2) fission from a rapidly rotating Earth and (3) capture by Earth after formation elsewhere in the solar system. The magmatic history of the Moon was also the subject of much debate. Many thought the Moon had remained relatively cool throughout its history and may even be the chondrite parent body. The disagreement continued until the return of the first lunar samples by Apollo 11. Although mostly consisting of soil samples, it became apparent very early on that the Moon had a complicated magmatic history. Fragments of anorthosite had a ubiquitous positive Eu anomaly, permeated the sample collection from each landing site and were interpreted as samples of the primary lunar crust. Fragments of basalt were found to be younger than the anorthosites and were determined to be samples of flood basalts that filled in large basins and formed the dark “mare” terrains, predominantly found on the near side. In addition to wildly varying compositions, such as TiO_2 contents ranging from 0.22 – 17 wt. %, they ubiquitously had a negative Eu anomaly and plagioclase nowhere near their liquidi. Combined with the observation of a seemingly global anorthosite crust, a model of a Moon that melted to great extents, perhaps even completely, arose in which the ferroan anorthosites were formed by floating on a Moon-wide magmasphere. The mare basalts were interpreted to be partial melts of a lunar mantle complementary to the anorthosite crust, formed from a common reservoir that had experienced removal of the crustal plagioclase, imparting the distinctive negative Eu anomaly. To explain the energy required to at least partially melt an entire planet, and also the moment of inertia of the Earth-Moon system, a model of lunar formation via impact of early Earth by a Mars-sized proto-planet emerged. Since Apollo, both the giant impact and LMO hypotheses have withstood scrutiny and become the widely accepted explanations for the formation and differentiation of the Moon.

The LMO hypothesis has, in the broadest sense, remained fairly static since its inception in the early 1970’s. Crust formation by flotation of plagioclase and the mare basalt source region forming from the complementary mafic cumulates have remained the canonical view. However, as would be expected, increasingly detailed and thorough examination of the sample collection has created not only a model significantly more complicated, but also a model whose details are still very much the topic of debate. In spite of this, a more detail model of lunar differentiation that is generally accepted by the community has evolved.

After lunar accretion from the debris disk surrounding early Earth resulting from the giant impact, the Moon is at least partially molten. The initial depth of lunar melting is still disputed, with estimates ranging from ~250 km to whole Moon melting (although the average estimate of initial LMO depth from the literature seems to have increased with time). Core formation is also still a subject of debate. Orbital data suggest a small core, but the Apollo seismic data are inconclusive. In any case, the bulk composition of the LMO is assumed to be representative of the bulk composition of the silicate Moon. Since the 1970's, many compositions have been proposed in the literature. They differ from each other most notably in terms of Mg* (molar Mg/(Fe+Mg) x 100), Fe content, and refractory lithophile element content. In recent years, debate has boiled down to primarily refractory element content, with one end-member composition positing that the Moon has essentially the same refractory element (i.e. Al, Th) content as the bulk Earth with the other end member holding that the Moon is enriched in such elements by a factor of 1.5 relative to Earth.

The actual crystallization and differentiation of the Moon has been modeled by numerous authors. No matter how deep the LMO is taken to be or what its precise composition is, the earliest formed crystals are always very rich in Mg and are dominated by olivine. What physically happens to these growing crystals in the early going is another matter. Most models have assumed the LMO solidified by means of crystal fractionation. This assumption usually stems from the models being geochemical in nature, with little or no consideration of magma ocean geophysics, and observations from the sample collection that imply chemical fractionations were occurring/had occurred when the source regions of mare basalts were forming. Some geophysical models for LMO crystallization suggest that up to even the first half of solidification may have been under equilibrium conditions, achieved by means of crystal suspension in a turbulent convecting ocean that prevents significant deposition and chemical isolation of early formed phases, even if geochemical data suggest it occurred. A reconciliation between these two types of models has yet to be realized.

Although olivine dominates the early crystalline phase assemblage and low-Ca pyroxene is usually assumed to follow, the presence or absence of garnet in the lunar mantle has received some notable attention. Though no basalt has yet been found in the sample collection that shows the clear signature of heavy Rare Earth Element (HREE) depletion caused by garnet retention in the source, a lunar mantle containing garnet would prove informative about the extent of initial lunar melting and the bulk composition of the magma ocean. In any case, as solidification proceeds, the cumulates become more OPX- and Fe-rich, reflecting the evolving composition of the LMO liquid. Not only is the LMO becoming Fe-rich, but also more Al-rich. Somewhere late in the crystallization sequence, ~75% solid according to most models, plagioclase begins to crystallize and float on the surface, owing to a density contrast with the progressively more Fe-rich magma ocean it grows out of. The plagioclase crystal structure will more strongly incorporate divalent Eu over the other trivalent REE's and imparts a negative Eu anomaly on the chondrite normalized REE pattern of the liquid it crystallizes and is removed from. The mafic olivine – OPX cumulates forming at the same time will inherit this Eu depleted REE pattern, a process that is later evidenced by the same pattern being present in the partial melts of these cumulates, the mare basalts.

However, none of the phases crystallizing up to this point (with the exception of the hypothetical garnet) take up significant quantities of REE's and other generally incompatible elements. Accordingly, these elements are being concentrated in the residual magma ocean liquid as it solidifies. Around 95% solid in most models, Fe and Ti enrichment in the liquid results in ilmenite saturation. This generates a layer of cumulates that is extremely dense relative to the rest of the cumulate pile below it. Meanwhile, the liquid left after ilmenite removal is becoming even more enriched in elements like potassium (K), the Rare Earth Elements (REE) and phosphorus (P). This distinctive incompatible element enrichment is referred to as KREEP and is found almost exclusively in a region on the near side of the Moon known as the Procellarum KREEP Terrane. KREEP is thought to represent the final dregs of the LMO, formed as it finished cooling. However, generation of the diverse mantle source regions for lunar basalts does not end with the final solidification of the LMO. The gravitational instability in the cumulate pile mentioned above has been proposed as the cause of mantle overturn, with the results being a redistribution and mixing of late stage, dense, sometimes Ti- and KREEP-rich cumulates and early, hot, less dense, Mg-rich cumulates in the lunar mantle. The mixing is far from homogenous, though, and creates a very heterogeneous mantle with the diverse collection of source regions implied by wildly varying basalt compositions.

The series of events detailed above is generally accepted in the lunar petrology community and comes from both sample observations (i.e. near-liquidus basalt phase relations, trace element and isotope concentrations, major element variations in basalts, etc.) and empirical modeling of LMO crystallization. The LMO has become the paradigm under which all new lunar data are interpreted. However, despite 40 years of investigation, the hypothesis has never been put to the test experimentally. The goal of this project was to finally test the LMO hypothesis with a coherent set of high-pressure experiments and a realistic model of how the LMO may have crystallized. Both refractory element enriched and non-enriched compositions were tested, effectively simulating magma ocean crystallization twice. Interpretation of the experimental results focuses on the early formed cumulates and the implications for later magmatism. The issue of whether garnet is in the mantle is addressed as well as the differences in mantle mineralogy produced by each type of bulk Moon composition. The cumulate pile is also considered as it relates to the source regions of subsequent lunar magmatism. The source regions of the low-Ti picrite green glasses and the highlands magnesian suite are discussed in detail. The picrite glasses are some of the most studied basalts from the Moon and the Mg-suite is a still-mysterious series of ancient plutonic rocks with contradictory primitive major element compositions and highly evolved trace element compositions.

The experiments presented below are the first of their kind and are aimed to help resolve some of the outstanding issues in lunar science related to magma ocean crystallization. They are also designed to provide a basic test of the hypothesis and whether the current models of crystallization and bulk composition can actually give rise to the lithologies seen in the sample collection. Tested below is an end member model of magma ocean crystallization featuring early equilibrium crystallization instead of a model of purely crystal fractionation. The results may suggest one style of differentiation over the other. It is also my hope these experiments can provide a foundation for future work on this topic.

1. INTRODUCTION

Analysis of the samples returned by the Apollo and Luna missions has revolutionized our understanding of the origin and evolution of the Earth-Moon system. In addition to shedding light on the origin of the Moon (e.g. Canup, 2004), multiple lines of evidence have led to the hypothesis that the Moon differentiated through a process of planetary-scale melting referred to as the Lunar Magma Ocean (Wood et al., 1970; Smith et al., 1970). Crystallization of the Lunar Magma Ocean (LMO) produced a wide variety of mafic lithologies in a heterogeneous mantle and a ferroan anorthosite crust via flotation of less-dense plagioclase-rich cumulates (Warren, 1985). Lunar scientists have, in most cases, been successful in placing the diverse lithologies present in the sample collection in the context of the LMO paradigm, whether as direct LMO crystallization products such as ferroan anorthosites, or as partial melts of differentiated mantle materials such as the mare basalts. Magma oceans have now been invoked on the basis of sample and remote sensing observations to explain the differentiation and lithological diversity of other terrestrial bodies such as Earth, Mars, Mercury and 4 Vesta (e.g. Ohtani, 1985; Tonks and Melosh, 1993; Li and Agee, 1996; Righter and Drake, 1997; Borg and Draper, 2003; Riner et al., 2009). However, large terrestrial planets at least partially obliterate the original products of their differentiation through post-magma ocean processes (i.e. plate tectonics on Earth) and meteoritic samples are delivered to us without crucial geologic provenance, making an accurate and detailed reconstruction of early planetary differentiation somewhat problematic. The Moon, however, with a lack of more recent geologic activity and being the only other planet from which we possess samples of a known geologic context, remains the perfect “case study” in the differentiation of planetary bodies.

Because magma oceans are thought to drive the chemical differentiation of large terrestrial bodies and set the stage for future magmatism, numerous authors have attempted to model the crystallization of magma oceans on the Moon (e.g. Taylor and Jakeš, 1974; Longhi, 1980; Tonks and Melosh, 1990; Snyder et al., 1992; Longhi, 2003) and other planets (e.g. Borg and Draper, 2003; Elkins-Tanton et al., 2003b; Brown and Elkins-Tanton, 2009). These models have, in general, taken two end-member forms: fractional crystallization from start to finish and a "two-stage" model of early equilibrium crystallization followed by fractional crystallization of the residual magma ocean. Both types produce broadly similar results for the Moon (Taylor and Jakeš, 1974; Snyder et al., 1992). Mg-rich olivine is the first phase to crystallize, followed by orthopyroxene, which creates a dunite and/or harzburgite lower mantle. Anorthitic plagioclase begins to crystallize late (roughly 75% solid) and floats to the surface of the magma ocean, forming the primary lunar highlands crust. The complementary mafic cumulates become more basaltic (and Fe-rich) in composition as crystallization proceeds and a very dense ilmenite-rich layer forms at about 95% solidification. The final residual LMO dregs becomes enriched in potassium (**K)**, rare earth elements (**REE)**, and phosphorus (**P**), amongst other incompatibles, and are typically referred to as urKREEP (Warren and Wasson, 1979; also see review by Shearer et al., 2006a). The progressively denser, cooler and more Fe-rich cumulates on top of the cumulate pile lead to a gravitational instability in the mantle. It has been suggested that this instability leads to overturn of the cumulate pile (Hess and Parmentier, 1995; Elkins-Tanton et al., 2002), resulting in varying degrees of mixing and/or relocation of early- and late-stage LMO cumulates. These cumulates, or mixtures thereof, are thought to be the source lithologies for the very diverse range of secondary lunar magmatism (e.g. Longhi, 1992a; Neal and Taylor, 1992; Hess and Parmentier, 1995; Shearer and Papike, 1999 amongst many others).

However, even after over 40 years of rigorous and insightful investigation, many questions about the magmatic evolution and internal structure of the Moon persist. Attempts have been made to constrain the bulk composition of the Moon (and by inference the LMO), yet debate remains as to whether the Moon is enriched in refractory lithophile elements (i.e. Al, Th) relative to Earth (Longhi, 2006; Taylor et al., 2006). Even relatively modest variations in the bulk composition of the Moon, as shown below, can have substantial effects on the outcome of LMO solidification models and, subsequently, the constitution of the lunar mantle (i.e. the presence or absence of garnet). The extent of initial lunar melting also remains a mystery, with estimates ranging from a shallow LMO (~250 km) up to whole Moon melting (Warren, 1985; Pritchard and Stevenson, 2000; Longhi, 2006). Intimately related to this are questions about the structure of the lunar mantle, the nature of the 400 km seismic discontinuity and the role the LMO played in dictating the nature of both (see review by Wieczorek et al., 2006). These problems are compounded by an incomplete understanding of the relationship of both mare and pre-mare magmatism to cumulate source regions in the mantle. The origin of the highlands magnesian-suite (or simply Mg-suite), a series of enigmatic ancient plutonic rocks featuring primitive major element, yet evolved trace element compositions, remains particularly problematic; although progress in understanding potential source regions in the context of the LMO is being made (e.g. Hess, 1994; Shearer and Papike, 2005; Longhi et al., 2010; Elardo et al., 2010).

This study revisits crystallization of the Lunar Magma Ocean in light of updated constraints on the bulk composition of the silicate Moon (Longhi, 2006; Taylor et al., 2006) and evidence suggesting that initial lunar melting may have been extensive to whole-Moon (Pritchard and Stevenson, 2000; Canup, 2004; Longhi, 2006). It is also the first attempt to experimentally simulate crystallization of the LMO and the first to model solidification of a whole Moon magma ocean. In order to place better constraints on the problems mentioned above, amongst others, we have investigated two end-member bulk Moon compositions using the "two-stage" model of magma ocean crystallization. This study will examine the first stage of this model: early solidification under equilibrium conditions and the implications for early LMO cumulates, the composition of the lower mantle, the degree of initial lunar melting and possible source lithologies of the Mg-suite.

2. EXPERIMENTAL AND ANALYTICAL METHODS

2.1 Crystallization model and experimental design

2.1.1 Convective flow and crystal suspension

Crystallization of the LMO has generally been modeled in two ways: crystal fractionation from start to finish and early equilibrium crystallization followed later by crystal fractionation. The former model has commonly been proposed based on geochemical arguments; however the latter "two-stage" model combines geochemical observations with geophysical models of large-scale cooling magma bodies. Thus, the crystallization model investigated here is based on such "two-stage" models as those proposed for the Moon by Tonks and Melosh (1990), Spera (1992), and Snyder et al. (1992). This type of crystallization model can be reasonably derived from convective flow theory for a system undergoing unsteady, high Rayleigh number convection, with the Rayleigh number (Ra) simply being the ratio of forces that drive convective flow to the forces that suppress it. Estimates of the Rayleigh number for a planetary-scale magmasphere are about 10^{24}-10^{29} (Tonks and Melosh, 1990). For comparison, Earth's subsolidus mantle has an Ra of about 10^{6}-10^{7} (Schubert, 1979). Once inertial forces are considered, a model of convection emerges that features a large, turbulent inertial flow zone bounded on top and bottom by smaller scale viscous sub-layers (Figure 1-A).

The capacity of the system to suspend crystals in the convecting liquid is primarily a function of the Rouse number, which is simply the ratio of terminal velocity of a crystal to the effective friction velocity of the melt. If the Rouse number (S) is greater than one, a crystal will settle, and if it is less than one, it will remain suspended. Tonks and Melosh (1990) modeled a 400 km LMO and showed that S was initially less than one for small crystals (<1 cm), assuming olivine was the only phase crystallizing for the first 50% of crystallization. With increasing degrees of crystallization, however, their model indicated that the magma would actually be able to suspend progressively larger crystals because SiO_2 enrichment in the melt would increase melt viscosity (hence decreasing S for a given crystal). Crystal suspension in the melt (equilibrium crystallization) will proceed until the crystals grow large enough to overcome convective forces (S > 1 for those crystals), the inertial flow zone disappears, and/or the crystal lock-up point is reached and turbulent convection is no longer possible. Tonks and Melosh (1990) estimated that this process might continue until approximately 50% solidification. This value differs significantly from the value of 78% assumed by Snyder et al. (1992) in their LMO crystallization model. The more conservative value of 50% solid proposed by Tonks and Melosh (1990) is used to calculate the composition of the early cumulate pile in this work. However, the results of equilibrium crystallization experiments up to ~78% solid will be considered below for comparison with the empirical results of Snyder et al. (1992). Although some crystal fractionation may occur in the lower viscous sub-layer, perhaps due to crystals growing large enough to overcome convection, it is likely insignificant and will not be considered further for the sake of assessing the viability of the "two-stage" model. See Tonks and Melosh (1990) and Spera (1992) for a much more thorough explanation and review of the principles presented above.

2.1.2 The adiabat and crystal nucleation

A second assumption made here is that the adiabat lies between the solidus and the liquidus at all depths in the LMO column (Figure 1-B) for the first 50% of crystallization and that its slope does not change appreciably. This assumption appears reasonable for the Moon because the slopes of the liquidus and solidus (dT/dz, where T is temperature and z is depth) for a peridotite composition are higher than for Earth or Mars due to the Moon's lower acceleration of gravity and, subsequently, because the pressure range for the Moon (4.7 GPa maximum, (Kennedy and Higgins, 1975)) is significantly less than for Earth and Mars. In the case of larger planets, one possible model posits that as the magma ocean cools, the adiabat could lie above the liquidus at shallow depths and cross it deeper in the magma ocean column (although other scenarios are certainly possible). This principle would constitute, in essence, the bottom-up crystallization and the adiabat assumed in the model of magma ocean crystallization on Mars in the work of Elkins-Tanton et al. (2003b) and is shown in Figures 1-C and D. Bottom-up crystallization was also suggested for a whole Earth magma ocean by Miller et al. (1991), although as the terrestrial magma ocean becomes more crystalline, the system becomes far more complicated (i.e. olivine neutral buoyancy zone). Liquidus inflections due to high pressure phases also become relevant for larger planets (Tonks and Melosh, 1990; Miller et al., 1991), but this is not the case for the Moon, which has a core pressure of only ~4.7 GPa.

Although the slopes of magma ocean adiabats can change as the system evolves (Miller et al., 1991) and this would have direct effects on crystal nucleation, here the assumed adiabat remains roughly parallel to the (simplified) LMO liquidus and solidus for the first 50% of crystallization. This is a simplification of the behavior of magma ocean adiabats, but it is necessary for the straightforward interpretation of experimental data and assessment of the "two-stage" model. The practical implications of this are that crystals can nucleate anywhere in the LMO column, and they will not subsequently dissolve when carried to different depths by turbulent, convective flow. In the case of a magma ocean on Earth or Mars with the adiabat shown in Figure 1-D, crystallization would occur only below the depth at which the adiabat crosses the liquidus and any crystals swept above this depth would dissolve.

2.1.3 Experimental design

Given the reasonable assumptions that crystallization can occur at all depths in the LMO and equilibrium crystallization occurs up to approximately 50% solidification, the crystallization sequence at all LMO depths must be investigated, as crystals grown throughout the column will eventually settle and contribute to the cumulate pile. However, to enable comparison with the empirical model of Snyder et al. (1992), we have chosen to conduct phase equilibrium experiments down temperature from the liquidus to ~80% solid at 0.5, 1, 2 and 4 GPa (representing ~100, 200, 420 and 1100 km depth, respectively). This will simulate solidification throughout the LMO column in an initially entirely molten Moon. A few experiments have been conducted near or below the solidus simply to identify the phases present in the subsolidus assemblage. Once complete, the experimental liquid compositions from the 1, 2 and 4 GPa experiments that contain approximately 50% liquid are used to calculate the residual magma ocean composition. The solid cumulate composition (+3% instantaneous trapped residual liquid of the same composition as the 50% residual LMO) is calculated from the minerals in these experiments to gain insights into the composition of the cumulate pile. The contribution from each pressure is weighted in both calculations to account for the volumetric difference of 50% solid or liquid at a given depth stemming from decreasing lunar radius at depths representing 1 GPa vs. 4 GPa, for example.

Two end member bulk compositions were used to experimentally simulate crystallization of the LMO: the Taylor Whole Moon (TWM) composition proposed by Taylor (1982) and the Lunar Primitive Upper Mantle (LPUM) composition proposed by Longhi (2003; 2006). Both compositions had ~250 ppm each of Ni, Co, Y, and V added to investigate partitioning behavior of these trace elements under LMO conditions. The TWM represents a Moon that is enriched in refractory lithophile elements (i.e. Al) by 50% relative to the LPUM composition and the bulk Earth (see Taylor et al. (2006) and Longhi (2003; 2006) for a review of arguments for each composition). Another significant difference is in Mg* (molar Mg/(Mg+Fe) x 100), with the TWM composition having an Mg* of 84 and the LPUM having an Mg* of 90. Many bulk Moon compositions have been proposed by various authors, but the TWM and LPUM represent end-member compositions due to the criteria above. Compositions are listed in Table 1.

Neither composition is assumed *a priori* to be more likely to represent the bulk silicate portion of the Moon; however, the experimental results below may prove insightful in resolving this disagreement.

2.2 Starting materials

The TWM and LPUM starting materials for this study were partially crystallized glasses made at NASA Johnson Space Center from anhydrous, dried, and powdered reagent-grade oxides and carbonates. Compounds were mixed in the desired proportions, except for Fe_2O_3, of which an additional 5 wt. % was added to compensate for Fe-loss to the Au-Pt crucible used for melting. The mixture was ground under acetone in an agate grinder, dried, and then placed in the Au-Pt crucible for melting in a Lindberg furnace. The mixtures were melted in air at ~1500° C for 4 hours and quenched in water. The resulting glasses were crushed, dried, and reground in the agate grinder. The TWM and LPUM compositions from Taylor (1982), Longhi (2003; 2006) and those used in this study are listed in Table 1.

2.3 Experimental Methods

All experiments reported here were conducted under nominally anhydrous conditions within high-purity graphite capsules with press fit lids produced at Arizona State University. Both starting materials and capsules were stored in a dessicator until use. Experiments were pressurized cold and then heated while maintaining pressure. The starting material was allowed to melt at superliquidus conditions for 10-15 minutes before being quickly cooled to the temperature of interest. Runs from 0.5 to 2 GPa were conducted using a Depths of the Earth QUICKPress non-end loaded piston cylinder apparatus at the Institute of Meteoritics. A -11.3% friction correction, which was previously determined for this apparatus in this lab, was applied to achieve the desired pressure. These experiments were run in talc-Pyrex cells with graphite heaters produced by Ceramic Substrates. Temperature was monitored using a W5Re-W26Re thermocouple and was maintained using a Love Self-Tune controller. Runs at 4 GPa were conducted in a Walker-style multi-anvil press at the Institute of Meteoritics using procedures, cell assemblies, and calibrations described by Agee et al. (1995). Cells were ceramic octahedra made to fit tungsten carbide cubes with edges truncated to an 8mm length and were stored at 110° C in a drying oven until use. The W/Re thermocouple was inserted radially at the center of the heater near the capsule. The capsule was separated from the Re foil heater by an alumina sheath. Temperature was controlled using a Eurotherm 3504 programmable controller. At completion of an experiment, runs were quenched by cutting power to the heater and the temperature typically dropped below the glass transition in <10 seconds. Capsules were then mounted in epoxy and polished flat for electron microprobe and SIMS analyses.

2.4 Analytical conditions

2.4.1 Electron microprobe conditions

Run products were analyzed for major and minor elements using a JEOL JXA 8200 Superprobe at the Institute of Meteoritics. Analyses were done using an accelerating voltage of 15 keV and a beam current of 20 nA. A 1 μm spot size was used on crystalline phases and a defocused, 10 μm diameter beam was used to analyze quenched melt. Standards were natural and synthetic minerals and Ni-, Co-, and V-metal. Peaks were counted for 30 seconds and backgrounds for 15 seconds for Si, Ti, Al, Fe, Mn, Mg, Ca, Na, and Cr, while 40 second peak counting times and 20 second background counting times were used for K, P, Ni, Co, Y, and V. Mineral compositions reported here are based on the average of 8-12 analyses and quench compositions on the average of 10-15 analyses.

2.4.2 Ion microprobe conditions

Ni, Co, Y and V were analyzed in select experimental run products using the Cameca ims 4f operated by the Institute of Meteoritics. Analytical conditions closely matched those used by Shearer and Papike (2005). A primary O^- ion beam was accelerated through a nominal potential of 10 kV. A 15 nA beam current was used with a spot size of ~15 μm. Sputtered secondary ions were energy filtered using a sample offset voltage of 105 V. Analyses involved repeated cycles of peak counting and included counting on a background position to monitor detection noise. Absolute concentrations were calculated using empiric relationships of trace element/$^{30}Si^+$ ratios (normalized to known SiO_2 content) to element concentrations as derived from calibration. Calibration curves were constructed using two glass standards, two olivine standards and one pyroxene standard.

3. RESULTS

The results of phase equilibrium experiments on the TWM and LPUM compositions (Table 1) are shown in temperature vs. pressure phase diagrams in Figure 2, with approximate liquidus, solidus and mineral-in curves for each. Experimental conditions, mineral and melt compositions, mineral/melt proportions and relevant partition coefficients are listed in Tables 2 and 3. Mineral-melt proportions were determined by least squares mass balance. The weighted compositions of the cumulate piles (Figure 4) and residual melts after removal of 50% solid are listed in Table 4.

Appendix A shows two backscattered electron images of typical experimental run products. Appendices B and C list the averages of electron microprobe analyses for each phase in each experiment and Appendix D lists the results of SIMS analyses for run products analyzed by that technique.

3.1 Taylor Whole Moon phase relations

Not surprisingly for a peridotite, the TWM composition has Mg-rich olivine (~Fo_{94}) as the liquidus phase at all relevant LMO pressures. Olivine persists as the only crystallizing phase down temperature until ~40-50% solid. At 2 GPa, low-Ca pyroxene (En_{87}; referred to as OPX hereafter) joins the assemblage as the second phase, consistent with various empirically predicted crystallization sequences (e.g. Snyder et al., 1992). However, at both 1 and 4 GPa, departures from this expected sequence are observed. At 1 GPa, an Al-Cr-spinel is the second phase to crystallize, though it remains low in modal abundance ($\leq$ 3%) with decreasing melt fraction. OPX (En_{82}) is the third phase to crystallize at 1 GPa and when it does, some olivine resorption may be observed at both 1 and 2 GPa. Olivine resorption is suggested by a decrease in the modal abundance of olivine when OPX begins to crystallize. At 4 GPa, Mg-Al-rich garnet (Py_{81}) begins to crystallize simultaneously with OPX (En_{89}) within the temperature resolution of the multi-anvil press. The Cr contents of the olivine are shown in Figure 5. The OPX Al_2O_3 contents range from 4.04 – 7.49 wt. % (Figure 6) and Cr_2O_3 contents from 0.39 – 1.86 wt. % (Figure 7). A high-Ca pyroxene (CPX hereafter) is observed near the solidus at 0.5, 1 and 2 GPa, making the sub-solidus assemblage a spinel lherzolite at low pressure and a garnet lherzolite at high pressure, which is not unexpected and consistent with previous studies (e.g. Stolper, 1980; Longhi, 1992a). However, equilibrium experiments near the solidus bear little relevance to LMO cumulates since crystal fractionation will have begun long before that point. Also, since attainment of equilibrium in such experiments is questionable (see section 3.4), experiments approaching the solidus are considered further only in terms of phase identity (i.e. CPX is present, but not plagioclase). In no experiment, even those beyond 78% solid, is plagioclase or ilmenite observed. The weighted residual LMO is listed in Table 4. It has an Mg* of 74.3, Al_2O_3 and CaO contents of 11.55 and 9.14 wt. %, respectively, and a CaO/Al_2O_3 of 0.79.

3.2 Lunar Primitive Upper Mantle phase relations

The LPUM composition also has Mg-rich olivine (~Fo_{96}) as the liquidus phase at all relevant LMO pressures. Olivine persists as the only crystallizing phase until ~50 – 60% solid. At 1, 2 and 4 GPa, OPX ($En_{89\text{-}92}$) is the second phase to crystallize, which is consistent with empirical crystallization models (e.g. Snyder et al., 1992), but in contrast to the TWM composition (Figure 2). Some olivine resorption may be observed with the appearance of OPX. No spinel phase is observed in the phase assemblage at any pressure. Garnet (Py_{82}) does crystallize at 4 GPa, however it enters the assemblage at ~70% solid, which is later than its entry point for the TWM and it appears in lower modal abundances. The Cr contents of the olivine are shown in Figure 5. The OPX contains Al_2O_3 ranging from 2.00 – 3.91 wt. % (Figure 6) and Cr_2O_3 ranging from 0.45 – 1.86 wt. % (Figure 7), making the OPX less aluminous than OPX from the TWM but similar in Cr_2O_3. CPX is observed near the solidus at 4 GPa, making the subsolidus assemblage a garnet lherzolite at high pressure. This observation, combined with the observation of CPX near the solidus at 0.5, 1 and 2 GPa in the TWM, makes it likely that CPX is present in the equilibrium sub-solidus assemblage for both compositions at all relevant pressures, although this is of little consequence to LMO crystallization models. The subsolidus assemblage for the LPUM at low pressure appears to be a lherzolite with no aluminous phase. As with the TWM, neither plagioclase nor ilmenite is observed in any experiment. The weighted residual magma ocean composition is listed in Table 4. It has an Mg* of 81.5, Al_2O_3 and CaO contents of 7.94 and 6.10 wt. %, respectively, and a CaO/Al_2O_3 of 0.77.

3.3 Trace element partitioning and oxygen fugacity

Ni and Co were added to the starting compositions in trace amounts (~250 ppm) to investigate their partitioning behavior in olivine as the LMO evolves chemically. The partition coefficients (D = concentration in mineral/concentration in melt) of each as a function of Mg* are shown in Figure 9. Cobalt initially starts off as incompatible at the highest Mg*'s, however, it shows a modest, but clear upward trend as the olivine becomes more Fe-rich. The behavior of Ni is more ambiguous. The TWM Ni partition coefficient data (Figure 9) suggest a steeper upward trend, but it is far less defined than the trend for Co and there is considerable scatter in the data. Three TWM experiments were analyzed by SIMS and there is excellent agreement between the two techniques for Co, but some disagreement for Ni. The SIMS derived partition coefficients for Ni are lower than the EPMA data suggests. The EPMA data for the LPUM are much more scattered and display no apparent trend. The uncertainty in the behavior of Ni may be due, at least in part, to Ni loss from the bulk composition to an unseen metal phase, which would bring the concentrations in both mineral and melt to below EPMA detection limits, making the EPMA data for Ni in Figure 9 questionable.

Y was added to both compositions in the same abundance because it can be used as a proxy for the mid to heavy Rare Earth Elements (REEs). As expected, Y is incompatible in olivine ($D_Y^{olivine/melt}$ ~0.008, from SIMS), OPX and spinel, but is compatible in garnet ($D_Y^{garnet/melt}$ 2.8 – 3.3, from EPMA). V was added to both compositions in the same abundance because V partitioning in olivine can be used to estimate the oxygen fugacity of the system (Shearer et al., 2006b). Based on SIMS-derived partition coefficients listed in Tables 2 and 3, the calculated oxygen fugacity in the experiments range from ~IW +1.5 to IW +2.0, consistent with previous studies of the oxygen fugacity imposed by oxygen reacting with the graphite capsule (e.g. Holloway et al., 1992). While the oxygen fugacity of lunar rocks is estimated to be lower than this (~ IW-1, Papike et al. (1998)), it is likely that in this range most Fe present in the melt is in the form of FeO, making the phase relations investigated here relevant to lunar systems. An experimental oxygen fugacity below the IW buffer would cause reduction of FeO to native Fe, thus changing melt composition and the subsequent phase relations.

3.4 Approach to equilibrium

The attainment of equilibrium in the experiments presented here was evaluated based on a few parameters. First was the value of the olivine-melt Fe-Mg exchange coefficient, K_D $((X_{FeO\text{-}Olivine})(X_{MgO\text{-}Melt})/(X_{FeO\text{-}Melt})(X_{MgO\text{-}Olivine}))$. The equilibrium value at 1 bar is equal to 0.30 (Roeder and Emslie, 1970), however the effect of pressure and composition, particularly MgO content, can alter what the equilibrium value is in a given system (Ulmer, 1989). The average value for both bulk compositions here was 0.33, so acceptable experimental values are considered to be in the range of 0.29 – 0.36. A few experiments fell outside the acceptable range (Tables 2 and 3). These experiments had low melt fractions (≤ 30 %), so it is possible that these experiments were not as close to equilibrium as would normally be desired. However, since these runs were not used in model calculations and thus do not affect the model results, they were accepted anyway.

Equilibrium was also assessed based on the degree of homogeneity in the phases present. No significant heterogeneity was observed in any of the experiments reported in Tables 2 and 3. However, heterogeneity, particularly in the clinopyroxene compositions, was observed in experiments that were near to or below the solidus. It is likely that such experiments would need days rather than hours to closely approach equilibrium, so these experiments are shown on the phase diagrams in Figure 2 to demonstrate the pressure and temperature conditions near the solidus and the identity of the phases in the near- and sub-solidus assemblages. Since these experiments are likely not as close to equilibrium as the runs with a higher melt fraction, they are not reported in Tables 2 and 3.

4. DISCUSSION

The crystallization products of the Lunar Magma Ocean have been extensively modeled by numerous authors and inferred from sample observations by numerous others. The experimental results reported here, the first of their kind, suggest that the lithologies produced by lunar differentiation are highly dependent on LMO composition and crystallization model (and its built in assumptions). A first order consequence of an LMO crystallization model that features turbulent convection, such as the one assumed in this work, is that growing crystals are entrained in the convection zone, in contact with the melt, maintaining equilibrium, until some other factor causes convection to wane and crystals to settle (see section 2.1.1). If the adiabat lies between the liquidus and solidus at all depths, as previously suggested for the LMO (Spera, 1992; Tonks and Melosh, 1990), the cumulate pile at the cessation of convection is made up of a combination of crystals grown at all depths. Snyder et al. (1992) assumed equilibrium crystallization until 78% solid in their model, however Tonks and Melosh (1990) argued that ~50% solid more likely represents the upper limit on the duration of equilibrium crystallization. Their arguments were based on calculations of the ability of a convecting magma ocean to suspend crystals as crystallization proceeds, crystal size increases and the stability of the inertial flow zone changes. They concluded based on these calculations that 50% solid was the upper limit on the duration of equilibrium crystallization and the calculations below use this value in order to test this end member model. The interpretations and calculations below also assume whole Moon melting, unless otherwise specified; however, if one wishes to consider a shallower LMO, the experiments conducted at pressures higher than those at the base of the preferred LMO simply need not be considered and appropriate adjustments to the calculations of the cumulate and residual liquid compositions need to be made.

The discussion below examines how the first 50% crystallization of the LMO dictates the composition and mineralogy of the deep mantle produced by two end member bulk Moon compositions. Also discussed are how these early cumulates could relate to the source regions of secondary lunar magmatism such as the Mg-suite and low-Ti picrite pyroclastic glasses, and how the LMO liquid composition after 50% crystal removal differs between the two starting compositions.

4.1 Mantle mineralogy, composition and the residual LMO

The differences between the TWM and LPUM bulk Moon compositions investigated here, namely refractory element enrichment and Mg* (TWM-84, LPUM-90), are stark enough to manifest themselves in the crystallization sequences and the mantle mineralogy produced for each, especially when whole Moon melting is considered (Figures 3 and 4). The TWM composition produces a Cr-rich spinel at low pressure (1 GPa, 200 km) that is not observed in the LPUM phase relations nor in most empirical models. Although both compositions crystallize garnet deeper in the LMO column, the TWM composition produces it earlier in the crystallization sequence and before the 50% cutoff point, meaning it would be present in the mantle. The appearance of spinel at low pressure and the earlier appearance of garnet at high pressure are very likely due to the elevated Al_2O_3 content of the TWM vs. the LPUM (6.1 wt. % vs. 3.9 wt. %, Table 1) and slight Cr_2O_3 enrichment in the TWM. The timing of OPX appearance between the two compositions is somewhat different, though the temperature resolution of the apparatus and gaps between data points make the appearance points shown in Figure 4 approximate.

Kesson and Lindsley (1976) suggested that that spinel phases observed by other workers in experiments on lunar compositions were products of the oxygen fugacity imposed by graphite capsules (IW+1-2, see above) and were not petrologically significant since the oxygen fugacity of lunar rocks is somewhat lower (~IW-1; Papike et al. (1998)). The Cr-spinel phase observed in these experiments is likely to be petrologically significant for a few reasons. First, the Cr-spinel is not observed in the LPUM phase relations at any point. By the time the Al_2O_3 content of the LPUM liquid reaches the level where the TWM began to crystallize spinel, OPX has entered the phase assemblage and depleted Cr_2O_3 from the melt enough to inhibit spinel formation. If oxygen fugacity was responsible, the spinel should still be expected to form at some point. Second, at 2 GPa, the TWM crystallizes spinel after OPX, even though OPX (and olivine) takes up components found in the spinel (i.e. Al_2O_3, Cr_2O_3, MgO, FeO). Thus, the spinel is likely a product of bulk composition and is therefore included in our calculations and interpretations. However, McKay et al. (2004) showed that oxygen fugacity had an effect on the composition of chromites produced in crystallization experiments on the Yamato 980459 martian meteorite composition. So, the precise composition of the spinel phase produced in these experiments may not truly reflect the composition of a spinel that might be produced in a LMO of lower oxygen fugacity. The high liquidus temperatures of the peridotitic bulk Moon compositions shown here preclude the use of a different capsule material (i.e. iron), which may shed light on the true composition of the spinel.

Crystallization of a deep or whole Moon LMO produces very different lower mantle mineralogy depending on whether the bulk silicate Moon is enriched in refractory elements (TWM) or not (LPUM). This difference will very likely be more pronounced in the later stage cumulates after significant olivine removal has magnified the differences between the bulk compositions in the residual liquid, but the early cumulate piles look very different as well, both in mineralogy and overall composition (Figure 3, Table 4). Cumulate pile compositions listed in Table 4 are calculated including 3% trapped instantaneous residual liquid of the composition of the residual after 50% crystal removal. The refractory element enriched TWM produces a lower mantle consisting of olivine ($Fo_{89.3}$), OPX ($En_{86.7}$), garnet ($Py_{81.3}$) and minor spinel from 1400 to 355 km depth (50% of lunar mantle volume, Figure 3). Somewhere between 2.5 and 3 GPa, there is a change in the identity of the stable aluminous phase (Stolper, 1980). Although the total cumulate pile will contain both spinel and garnet, spinel will be present only below these pressures and garnet only above. The LPUM produces a mantle with only olivine ($Fo_{92.9}$)

and OPX ($En_{92.3}$). The presence of garnet in LMO produced cumulates is particularly interesting, as much has been made of the presence or absence of garnet in the deep lunar mantle (e.g. Beard et al., 1998; Neal, 2001; Khan et al., 2006; Draper et al., 2006). The distinct HREE depletion signature attributed to garnet retention in the source has not been observed in basalts from the Moon nor is it a liquidus phase at any reasonable multiple saturation point for such basalts (e.g. Draper et al., 2006). It is possible that melting of the lower mantle simply consumed garnet, especially given that the TWM lower mantle contains relatively small amounts of it (3.2%), which would make detecting the presence of garnet in the mantle more problematic. It is also possible that garnet might be excluded from the lower mantle if equilibrium crystallization waned before garnet began to crystallize or if the LMO crystallized fractionally from the beginning. An extent of melting that consumed garnet is a distinct possibility and although models such as those proposed by Tonks and Melosh (1990) and Spera (1992) suggest a completely fractionally crystallizing LMO is unlikely, it is still possible. Another possibility is that the Moon is simply not enriched in refractory elements relative to Earth, as this would be enough to exclude garnet from early LMO cumulates (see below).

The LPUM lower mantle is not only more magnesian than the TWM lower mantle, but is also free of any aluminous phase and consists solely of olivine and OPX (Figure 3, Table 4). Even after the incorporation of 3% trapped instantaneous residual liquid (residual LMO compositions, Table 4), the LPUM lower mantle is depleted in Al_2O_3 by a factor of ~3 relative to the TWM lower mantle. The absence of garnet is more consistent with sample observations, but as discussed above, the presence of small amounts of garnet in the mantle cannot be fully ruled out and is not enough by itself to confirm or refute that the Moon is or is not enriched in refractory elements relative to Earth.

The residual magma ocean compositions after removal of 50% solid are listed in Table 4. These compositions approximate the composition of any trapped instantaneous residual liquid in the cumulate piles. Fractional crystallization of these compositions is expected to lead to dramatically different cumulates in the second half of LMO solidification. The first 50% crystallization has magnified the differences between the starting bulk compositions. The first area where the differences are apparent is in the Mg*'s, 74.3 vs. 81.5 for the TWM and LPUM, respectively. The compositions of the olivine, OPX and, most likely, the eventual CPX will echo this disparity, which will become even more enhanced down liquid line of descent by the removal process of fractional crystallization. The next, and perhaps most telling difference, is in the Al_2O_3 and CaO contents of the residual melts. The TWM residual has 11.6 wt. % Al_2O_3 and 9.14 wt. % CaO whereas the LPUM residual has 7.9 wt. % Al_2O_3 and 6.1 wt. % CaO. Although this will have the effect of making the pyroxenes slightly more enriched in these elements in the TWM late stage cumulates, where the difference will be most apparent is in the timing of plagioclase appearance. The TWM residual LMO will, in all likelihood, crystallize plagioclase earlier than the LPUM residual and in greater quantities, leading to a thicker primary crust. The crustal thickness produced by these two compositions could prove to be criteria for constraining the bulk composition of the Moon and/or the extent of lunar melting (i.e. if the TWM produces a plagioclase crust that is too thick, an initially entirely molten Moon cannot have a TWM bulk composition, or if it does, initial melting must have been less than complete). There is also a significant difference in the TiO_2 contents of the residual melts, with the TWM residual containing twice as much as the LPUM residual (0.61 vs. 0.30 wt. %). This will likely lead to earlier crystallization of ilmenite in the TWM residual in much the same fashion as plagioclase. These differences are also reflected in the CIPW norms or the residual liquids. The CIPW norms for both residual magma oceans after 50% crystallization are listed in Table 5, along with the norms of the residual magma oceans assuming equilibrium crystallization waned at 25 and 70 percent solid. In all three calculated residual LMO's, the norm calculations also show that the TWM residual is likely to crystallize plagioclase and ilmenite sooner and in greater quantities than the LPUM residual.

4.2 Crystallization sequence: Experimental vs. empirical

The empirical model of Snyder et al. (1992; "Snyder model" hereafter) assumed a shallow (400 km) LMO with an intermediate Al_2O_3 content (5 wt. %) and a slightly lower Mg* (82) than those investigated here, making their starting composition more similar to the TWM. They also modeled crystallization at only one pressure, 0.6 GPa (~120 km). Their crystallization sequence compared with the results of this study is shown in Figure 4, with the experimental results at 1 GPa being most analogous. There are significant differences between the 0.6 GPa empirical and 1 GPa experimental results; OPX has not joined the phase assemblage for either the TWM or LPUM compositions by 50% solid at 1 GPa, yet it has in the Snyder model. The Snyder model also does not produce a spinel phase, which is observed in the TWM crystallization sequence. If a shallow (~400 km) LMO and a 50% solid equilibrium crystallization cutoff is considered, the phases in the deep cumulates produced by each composition differ: The Snyder model results would still produce a deep mantle consisting of olivine + OPX, however olivine + spinel result from a TWM starting LMO, and the LPUM composition would produce only olivine. The trace element evolution would be similar for each, as the phases present do not take up significant lithophile trace elements such as the REE. If whole Moon melting is once again considered, the differences between the experimental results and the Snyder model become even more pronounced, most notably the inclusion of garnet in the TWM mantle and the OPX abundances in all.

Even for shallow magma oceans, crystallization models such as the Snyder model that do not consider the full range of relevant pressures and rely upon empirical approximations of phase relations may not adequately represent nature. They may exclude relevant phases from their solutions (i.e. Cr-spinel, garnet at high pressure) or otherwise provide a less than accurate picture of phase entry points, thus changing what mantle mineralogy is produced (i.e. OPX entry point, see above). Also, Snyder et al. (1992) assume equilibrium crystallization until 78% solid without presenting adequate reasoning as to why crystal suspension would last that long. Such an assumption will dramatically affect the liquid line of descent and composition of the cumulate pile. Even the 50% equilibrium crystallization cutoff point assumed here may result in a residual magma ocean too Mg-rich to produce the mare source regions. If shown to be the case, a fractionally crystallizing magma ocean such as those called upon by Longhi (2003) and Longhi et al. (2010) may need to be invoked. In any case, the empirical vs. experimental comparison demonstrates starting LMO composition, pressure effects and the geophysical details of the assumed crystallization model must be carefully considered when modeling crystallization of the LMO.

4.3 The highlands magnesian suite

The first episode of post-LMO basaltic magmatism and crustal growth on the Moon is represented by the plutonic cumulate lithologies of the Mg-suite. Emplaced at all levels of the LMO-derived crust between ~4.46 to 4.1 Ga (Nyquist and Shih, 1992; Shih et al., 1993; Snyder et al., 2000; McCallum and Schwartz, 2001; Edmunson et al., 2009), they are chemically distinct from the FAN's. However, partially overlapping ages with the FAN's and meteoritic bombardment combined with later overlying volcanism have clouded the details of the relationship between Mg-suite rocks and the primary lunar crust (Ryder et al., 1997; Snyder et al., 2000). Most Mg-suite rocks can be related to each other by the fractional crystallization sequence of dunite → troctolite → norite. The estimated parental melts had very primitive major element compositions and crystallized high-Mg* olivine (Fo_{95-90}) and orthopyroxene (En_{92-86}). In contrast to this, these magmas were co-saturated in high-Ca plagioclase (An_{97-94}) and had an enrichment of incompatible elements. The olivine in Mg-suite rocks also contain much lower Ni, Co and Cr relative to the more Fe-rich olivine found in the younger mare basalts (Shearer and Papike, 2005; Longhi et al., 2010).

The origin of Mg-suite parental magmas, with seemingly contradictory chemical features (primitive major elements, highly evolved trace elements), early co-saturation of Mg-rich olivine and Ca-rich plagioclase and low Ni, Co and Cr, has remained elusive. Shearer and Papike (2005) detailed five models previously proposed for the petrogenesis of the Mg-suite: (1) Re-melting and mobilization of KREEP, (2) melting of the KREEP metasomatized lower crust, (3) partial melting of progressively deeper LMO cumulates caused by heating of the KREEP horizon, (4) melting of KREEP hybridized sources in the deep mantle (4a) or near the base of the crust (4b), and (5) KREEP assimilation by rising, deep mantle melts. Models 1 and 2 can be ruled out because the Mg*'s of the Mg-suite parent magmas are too high to have come from late-stage LMO residual liquids and because the diversity and duration of basaltic magmatism with a KREEP signature suggests multiple mantle sources (Borg et al., 2004; Shearer and Papike, 2005). Model 3 indicates that early KREEP-rich basaltic magmas should have a lower Mg* than later KREEP-rich magmas (the upper cumulate pile is more Fe-rich than the lower pile), but the opposite relationship is observed and this model does not explain the variety of cumulates that melted and mixed with KREEP over the duration of lunar basaltic magmatism.

Models 4 and 5, however, can account for the diversity of compositions with a KREEP signature. These models are shown in Figure 8. In model 4a, the Mg-suite magmas form as a result of KREEP-rich material being brought to depth by overturn, hybridizing early, Mg-rich LMO cumulates. KREEP produces the heat that leads to partial melting. These melts then rise and assimilate FAN component at the base of the crust. In model 4b, early LMO cumulates are emplaced near the base of the crust via overturn where they mix in the solid state with KREEP. Subsequent partial melts are emplaced in the crust to form the Mg-suite. In model 5, the Mg-suite magmas can form either through partial melting of the deep, Mg-rich cumulates in the lower mantle or, more likely, from decompression melting of the same cumulates as they rise due to cumulate overturn (Hess and Parmentier, 1995). These melts assimilate KREEP and possibly FAN material at the base of the crust before emplacement.

In models such as 4 and 5, high Mg* melts form from early olivine ± OPX LMO cumulates. Since these cumulates are poor in REEs and Al_2O_3, and cannot form the Mg-suite by themselves, they interact with KREEP and crustal anorthosite to form the melts parental to the most primitive members of the Mg-suite (dunites and troctolites). The Mg* of the olivine in the dunites and troctolites can provide constraints on the Mg* of the parental melts and the source regions they were extracted from. The most primitive Mg-suite rocks contain olivine of the composition Fo_{95-90}, indicating parental melts with an Mg* of ~84 – 74 at near surface pressure. This means that even if the parental melts were extracted from the deepest cumulates formed in a whole Moon magma ocean, the pressure dependant Mg-Fe exchange equilibrium constrains the olivine in the source to have a minimum Mg* of ~89 (Ulmer, 1989; Hess, 1994) and to be much more magnesian that the mare basalt and picrite glass source regions (Elkins-Tanton et al., 2003a). Bulk Moon compositions offer little help in the search for just such a source region because their subsolidus assemblages are generally lherzolitic and undifferentiated mantle by itself would therefore likely produce tholeiitic melts, which are absent on the Moon and undersaturated in plagioclase when coexisting with olivine rich enough in Mg (Grove and Bryan, 1983), thus providing poor fits for the Mg-suite parent melts. There is also no isotopic or trace element evidence for melts originating from undifferentiated lunar mantle.

In terms of major elements and phases, the cumulate piles produced by the first 50% of LMO crystallization provide a much more reasonable fit for the required source regions. Both the TWM and LPUM compositions produce early cumulate piles that are predominantly OPX bearing dunites (Figure 3), have high overall Mg*'s (89.7 and 92.9, respectively) and contain 88% or more Mg-rich olivine ($Fo_{89.2}$ and $Fo_{92.9}$, respectively), meaning both cumulate piles fit the Mg-suite mafic component parental source region constraint of Mg* ≥ 89 (Hess, 1994), though just barely for the TWM cumulates. The temperatures of these early cumulates are also suggestive that they could act as the source regions for these melts. The temperature of the TWM cumulate pile ranges from ~1400° C to 1800° C from horizon to core-mantle boundary and the LPUM from ~1525° C to 1800° C. Models 4 and 5 require the deep LMO cumulates to be hot compared to the base of the crust. KREEP addition to the source region and/or decompression with overturn leads to partial melting (Figure 8). The near overlapping ages between some Mg-suite rocks and the end of magma ocean crystallization implies that deep cumulates will not have had time to significantly cool, so along with the chemical constraints detailed above, early LMO cumulates such as the ones produced in this study could potentially act as a component of the Mg-suite parental melt source lithologies.

The density of these cumulates also lends support to models 4 and 5. As expected and required by the cumulate overturn model, these early cumulates are less dense compared to later stage, ilmenite-rich cumulates. The density of the cumulate piles from this study is ~3300 Kg/m^3 while the density of the late stage ilmenite bearing cumulate consisting of 15% ilmenite and 85% CPX from the model of Hess and Parmentier (1995) is ~3700 Kg/m^3. This density contrast could facilitate overturn and partial melting of the early, hot LMO cumulates.

The low Ni, Co and Cr contents of the Mg-suite olivine compared to olivine from the more Fe-rich mare basalts is another distinguishing and enigmatic feature of their parental magmas. Longhi et al. (2010) summarized the nature of the discrepancy in detail and reviewed literature pertaining to Co and especially Ni partitioning in olivine. The vast majority of previous work on Ni and Co partitioning in olivine suggested that these elements should be very compatible and previous LMO models have concluded that early olivine LMO cumulates should be Ni- and Co-rich. However, on the basis of some previous work (e.g. Jones, 1984) and their own melting experiments and calculations for a fractionally crystallizing LMO, they concluded that Ni and Co would initially be slightly incompatible in olivine and then, as crystallization proceeds (and olivine Mg* decreases), Ni abundances in the LMO cumulate pile would go through a prominent maximum and then drop while Co would steadily increase. Ni and Co partitioning in olivine was measured in this study to provide a further test of this idea. A comparison of these results (Figure 9) with the results of Longhi et al. (2010) is shown in Figure 10, which shows both EPMA and SIMS derived partition coefficients as a function of percent solid with the fractional crystallization trends from the Longhi et al. (2010) calculations. As Mg* decreases with increasing crystal fraction, D_{Co} in olivine does increase from an initial value below unity (~0.8) to values from 1.5 – 2 by 50% solid, consistent with the results of Longhi et al. (2010) and Jones (1984). The behavior of Ni in olivine, however, is a bit more uncertain from the results above. While EPMA data for the TWM suggests D_{Ni} is inversely proportional to Mg* over the range investigated (Figure 9), as should be expected from the Longhi et al. (2010) results, there is considerable scatter in the data and the data for the LPUM composition are even more ambiguous. SIMS measurements, although few in number, suggest Ni loss in a few runs, perhaps to an unseen metal phase such as the phase observed by Longhi et al. (2010).

Regardless, the data presented here and the study of Longhi et al. (2010) suggest a mechanism for early, hot, less dense, Mg-rich LMO cumulates to be depleted in Ni and Co relative to the more Fe-rich mare basalt source regions (Figure 10), further suggesting that these cumulates could have acted as sources to a component of the Mg-suite parental melts. However, an important caveat is that if equilibrium crystallization proceeds to a point where the D_{Ni} in olivine becomes significantly elevated from its low value near the liquidus, calling upon a low D_{Ni} value as the reason for early LMO cumulates to be depleted in Ni becomes impossible. Unfortunately, the microprobe data presented above for D_{Ni} in olivine are too ambiguous to draw any major conclusions as to whether D_{Ni} is too high at 50% solid to produce a cumulate pile depleted enough in Ni to act as a source region for the Mg-suite parental magmas. If that is the case however, a fractionally crystallizing magma ocean that produces a cumulate pile zoned in Ni and Co, such as the one modeled by Longhi et al. (2010), may be required.

In terms of Cr, the TWM cumulates seem to be a poorer fit. Inclusion of the spinel phase, although in small modal abundances, may elevate the Cr abundances in a partial melt to unacceptably high values, especially if spinel is consumed. Also, OPX from 1 and 2 GPa and garnet in the TWM cumulate pile contain ~1.8 and 1.9 wt. % Cr_2O_3, respectively (Figure 7). The LPUM cumulates, however, contain no Cr-spinel or garnet, and the OPX contains less Cr_2O_3 (~0.5 wt. %). Cr_2O_3 in olivine produced by the two bulk compositions is similar (~0.2 – 0.35 wt. %, Figure 5). This is suggestive that, in terms of Cr, the LPUM cumulates provide a better fit for the source regions of the Mg-suite parental melts when considering the models above.

On the other hand, models that advocate early LMO cumulates as the source of a significant component of the Mg-suite parental magmas have severe problems. Even the minor aluminous garnet, spinel and small amounts (~3%) TIRL in the TWM cumulate pile is not enough to put plagioclase on the liquidus of a partial melt at low pressure, as required for troctolite petrogenesis. An additional source of Al_2O_3 is still required. This has been presumed to be crustal anorthosite assimilation in many models, but calculations by Hess (1994) suggested that there was not enough superheat available in Mg-suite parental magmas to assimilate the required anorthosite without inducing olivine crystallization that would reduce the Mg* of the melt to unacceptably low values. Also, in model 4a, KREEP is brought to depth by overturn and initiates melting. However, even though pristine KREEP shows the low Ti/Y ilmenite fractionation signature (Warren and Wasson, 1979), it is the late-stage Fe-, Ti-rich dense ilmenite-bearing LMO cumulates that drive overturn. It is difficult to envision how the more buoyant KREEP and the ilmenite-rich cumulates that immediately preceded its formation are sufficiently decoupled during overturn to result in deep sources for Mg-suite magmas rich in KREEP but low in Ti. Without KREEP addition or cumulate overturn, these early LMO cumulates will very likely be far too refractory to generate volumetrically significant basaltic partial melts on their own. This means models involving melting of the early LMO cumulates without KREEP addition or overturn can be ruled out. Decompression melting as a result of overturn combined with KREEP mixing or assimilation at shallower depths may be enough to generate partial melts and simultaneously explain the odd incompatible element compositions of the parental melts, but it still does not explain the absence of high-Ti Mg-suite rocks nor does it solve the anorthosite assimilation problem. Clearly more investigation and refinement of Mg-suite petrogenesis models is required, however the data presented above suggests that early LMO cumulates could act as the source lithologies for the high-Mg*, low-Ni, Co and Cr poor component of the Mg-suite parental magmas.

4.4 Low-Ti green glass source region

The various picrite glasses collected on the Moon are compositionally unlike any basalt yet sampled from another terrestrial body. With lower Al_2O_3 and CaO and higher MgO and FeO contents than typical terrestrial basalts, they compositionally have more in common with komatiites than basalts. They also exhibit TiO_2 contents ranging from 0.22 – 17 wt. % (Shearer and Papike, 1993), with the higher end unlike any other magma composition known in the solar system to date. They also appear to represent the best candidates for primary magmas of any "basalt" in the Apollo sample collection (Delano, 1986), especially the very low-Ti (VLT) glasses such as the Apollo 15 green glass suite. Consequently, they are among the most studied samples in the collection (e.g. Chen and Lindsley, 1983; Delano, 1986; Longhi, 1992a, b; Shearer and Papike, 1993; Elkins et al., 2000; Elkins-Tanton et al., 2003a; Draper et al., 2006; Longhi, 2006 amongst others). For these reasons and because the cumulate pile discussed in the preceding sections would physically encompass their source regions, this section focuses on the implications of the results above for the source regions of the Apollo 14 and 15 ultramafic VLT green glasses.

Studies of experimental phase relations have shown that the Apollo 14 B and Apollo 15 A-B-C green picrite glasses have points of multiple saturation (MSP) on their liquidi from ~260 km to ~480 km depth in the lunar mantle (Elkins et al., 2000; Elkins-Tanton et al., 2003a). All of the glasses have olivine and OPX at their MSP's. Assimilation or other modification processes would make these compositions somewhat less than truly "primary," so these depths should be viewed as an average (or at worst minimum) depth of melt segregation. Calculations by Longhi (2006) suggested that initial melting of LMO cumulates to generate these compositions could have extended as deep as 700 – 1000 km. Therefore, the source regions for the Apollo 14 and 15 VLT green glasses (with the exception of A15C if its MSP depth of 260 km is taken as the actual depth of melt generation) all fall inside the initial LMO equilibrium crystallization-generated cumulate pile described above, the top of which would be at a depth of ~355 km. It is useful then to consider these early LMO cumulates in the context provided by the green glass source regions.

Longhi (2006) modeled the source regions for the A15C green glasses and proposed two possible source region compositions: the first (GGSa) was dominated by olivine with some OPX and the second (GGSp) was dominated by OPX with some olivine. These compositions along with the compositions of the experimentally generated early cumulate piles for both bulk Moon compositions are shown in Table 4. By themselves, partial melting of the cumulate piles produced by 50% equilibrium LMO crystallization cannot produce the Apollo 14 and 15 green glasses. The experimentally produced cumulate piles are far too rich in MgO, too poor in FeO and, consequently, have too high an Mg* to be a reasonable match for even the olivine dominated green glass source region GGSa. The experimental cumulate piles have less than 9% OPX, so naturally they provide poor fits for OPX dominated source region GGSp as well.

To explain their major and trace element compositions, models of the petrogenesis of the Apollo 14 and 15 green glasses have invoked mixing of early and late LMO cumulates in the source, with shallower assimilation of a depleted cumulate for the Apollo 15 glasses (Elkins-Tanton et al., 2003a; Longhi, 2006) and KREEPy material for the Apollo 14 B glasses (Shearer and Papike, 1993; Elkins et al., 2000). Because the

Al_2O_3 and CaO contents of the green glass suite appear to be buffered at near constant values, a low-Ca pyroxene dominated source region (such as GGSp) has been proposed because (1) OPX appears at the green glass MSP's and (2) Al_2O_3 and CaO are not strongly incompatible in OPX, as they are in olivine. An OPX dominated source region would then buffer the Al_2O_3 and CaO content of partial melts over varying degrees of melting (Shearer et al., 2006a). If mixing of early and late LMO cumulates is responsible for the composition of the green glass source regions, on the surface the TWM cumulates seem to provide a better fit for the early cumulate contribution than do the LPUM cumulates. Incorporation of garnet and minor spinel into the cumulate pile make the early TWM cumulates very similar in Al_2O_3 content to the GGSa source, though still too poor in CaO. The presence of garnet and spinel in the cumulate pile, in addition to OPX with higher aluminum (Figure 6), suggests the TWM cumulates would be more fertile if aluminum is a melting flux during green glass parental magma production. Additionally, since the TWM residual LMO is significantly richer in Al_2O_3 than the LPUM residual LMO (Table 4), the composition of later stage low-Ca pyroxene will reflect that. However, problems with the TWM cumulate pile remain when examined in the context provided by the green glass. Experiments by Draper et al. (2006) on the A15C composition suggested that garnet, a constituent of the early TWM cumulate pile, played no role in the generation of the A15C green glasses. Also, the garnet produced by crystallization of the TWM is more magnesian ($Py_{81}Al_{11}Gr_8$) than the garnet near the A15C garnet-OPX MSP ($Py_{71}Al_{19}Gr_9$) found by Draper et al. (2006). The LPUM cumulate pile is a factor of ~3 lower in Al_2O_3 than the TWM cumulates and a factor of ~1.7 lower in CaO. So, though they are richer in MgO and poorer in FeO than the TWM cumulates, mixing of the late-stage, more aluminous OPX-rich cumulates with the early LPUM cumulates may provide a better opportunity to create a reasonable match with the GGSp and eliminates the need to explain away garnet.

5. CONCLUSIONS

Phase equilibrium experiments were conducted on the refractory lithophile element enriched Taylor Whole Moon composition (Mg* 84) and the Lunar Primitive Upper Mantle composition (Mg* 90). A Lunar Magma Ocean featuring whole Moon melting and a "two-stage" model of protracted equilibrium crystallization (as a result of crystal suspension and turbulent convection) up to 50% solid, similar to that modeled by Tonks and Melosh (1990), were used to calculate the composition of the early cumulate pile and residual magma ocean compositions.

A LMO of Taylor Whole Moon composition produces Mg-rich olivine as the only crystallizing phase over the first ~40 – 50% solid. The second phase to crystallize at 2 GPa (~420 km) is low-Ca pyroxene, which follows the predictions of numerous empirical models (e.g. Snyder et al., 1992; Longhi, 2003), however at lower pressure (1 GPa, 200 km) a Cr-spinel is the second phase to crystallize and at higher pressure (4 GPa, 1100 km) garnet and OPX enter the assemblage at virtually the same point. When a weighted average of the cumulates at each pressure after 50% crystallization is calculated, the lunar mantle from the core-mantle boundary at ~1400 km to the top of the cumulate horizon at ~355 km consists of 88.5% olivine ($Fo_{89.3}$), 7.8% OPX ($En_{86.7}$), 3.2% garnet ($Py_{81.3}$) and 0.5% Cr-spinel. The subsolidus assemblage at 0.5, 1 and 2 GPa consists of olivine, OPX, CPX and spinel (a spinel lherzolite). Between 2.5 and 3 GPa, the aluminous phase changes to garnet, making the subsolidus assemblage at 4 GPa a garnet lherzolite.

An LMO of Lunar Primitive Upper Mantle Composition also produces high-Mg olivine as the first crystallizing phase, up to ~50-60% solid. More in keeping with empirical models than the TWM, the second phase to enter the equilibrium assemblage at all pressures is OPX. Garnet is the third phase in at 4 GPa, however it begins to crystallize well after 50% solid. No spinel phase is observed at any pressure. When the same weighted average calculation is performed to calculate the composition of the deep mantle produced by an LPUM magma ocean is performed, it consists of 93.2% olivine ($Fo_{92.9}$) and 8.8% OPX ($En_{92.3}$). The subsolidus assemblage at low pressure for the LPUM is a lherzolite without an aluminous phase, but at 4 GPa garnet joins olivine, OPX and CPX in the subsolidus (garnet lherzolite).

The residual LMO compositions produced by removal of 50% solid have some stark differences. The difference in Mg* (TWM 74.3 vs. LPUM 81.5) will be strongly reflected in the composition of the olivine and pyroxenes that crystallize under fractional conditions later and presumably form the mare basalt source regions. The differences in Al_2O_3, CaO and TiO_2 will cause plagioclase and ilmenite to crystallize earlier for the TWM and will likely lead to a thicker primary crust. This could be used to place constraints on bulk lunar composition and the extent of initial melting.

Both the TWM and LPUM cumulate piles after 50% crystallization appear to have some features the source regions of the magmas parental to the Mg-suite. Although they are poor in incompatible elements and will not generate melts with plagioclase near the liquidus, both the bulk cumulate Mg* and the olivine Mg* match the constraints of Hess (1994) that source regions to troctolite parental melts must have an Mg* of ≥89. These cumulates would also be very hot (1400-1800° C) at the beginning of Mg-suite magmatism, implying that cumulate overturn could lead to decompression melting and melts with a high Mg*. They will also be poor in Ni and Co, another feature of Mg-suite parental melts. The olivine-liquid Ni and Co partitioning data presented above suggest agreement with the data of Longhi et al. (2010), who suggested that early formed olivine would be poor in Ni and Co compared to later formed olivine, which could resolve the discrepancy between Ni and Co contents of Mg-suite olivine and mare basalt olivine. However, the Ni partitioning data presented here are not conclusive enough to definitively say that the equilibrium cumulate pile after 50% crystallization will be low enough in Ni to act as the source region for a component of the Mg-suite parental melts. If it is not, a fractionally crystallizing magma ocean must be called upon (i.e. Longhi et al., 2010). The Mg-suite parental magmas also feature low Cr contents. For this constraint, the LPUM cumulate pile provides a better fit, as it contains no Cr-spinel, no garnet (containing 1.9 wt. % Cr_2O_3 in the TWM cumulates), and OPX from 1 and 2 GPa with a factor of more than 3 less Cr_2O_3 than TWM produced OPX.

Although the 50% cumulate piles for these compositions physically encompass the source regions for many of the varieties of low-Ti picrite green glasses, as determined from their olivine-OPX multiple saturation points (e.g. Elkins-Tanton et al., 2003a), the composition of the cumulate piles both provide poor fits for the estimated compositions of the green glass source regions (Longhi, 2006). Both the TWM and LPUM cumulate piles are too Mg-rich and too FeO-, Al_2O_3- and CaO-poor to provide reasonable matches. Even the addition of 3% trapped instantaneous residual liquid cannot bring the Al_2O_3 and CaO content of the cumulate pile to acceptable levels. Also, these cumulate piles are dominated by olivine. OPX dominated source regions are favored for the green glass source because OPX is the only phase that can be reasonably called upon that can buffer the Al_2O_3 and CaO content of partial melts to the observed values in the green glasses (Shearer et al., 2006a). To create the appropriate phase assemblage and composition for the green glass source at the appropriate depths, extensive mixing with later-stage LMO cumulates and/or a mantle produced by a fractionally crystallizing magma ocean must be invoked. Partial melts of undifferentiated mantle of either bulk composition explored here would likely produce melts of tholeiitic character, which are not observed anywhere in the sample collection.

6. REFERENCES

Agee, C.B., Li, J., Shannon, M.C., Circone, S., 1995. Pressure-temperature phase diagram for the Allende Meteorite. Journal of Geophysical Research 100 17,725-717,740.

Beard, B.L., Taylor, L.A., Scherer, E.E., Johnson, C.M., Snyder, G.A., 1998. The source region and melting mineralogy of high-titanium and low-titanium lunar basalts deduced from Lu-Hf isotope data. Geochimica et Cosmochimica Acta 62 525-544.

Borg, L., Draper, D., 2003. A petrogenetic model for the origin and compositional variation of the martian basaltic meteorites. Meteoritics and Planetary Science 38 1713-1731.

Borg, L.E., Shearer, C.K., Asmerom, Y., Papike, J.J., 2004. Prolonged KREEP magmatism on the Moon indicated by the youngest dated lunar igneous rock. Nature (London) 432 209-211.

Brown, S.M., Elkins-Tanton, L.T., 2009. Compositions of Mercury's earliest crust from magma ocean models. Earth and Planetary Science Letters 286 446-455.

Canup, R.M., 2004. Dynamics of lunar formation. Annual Review of Astronomy and Astrophysics 42 441-475.

Chen, H.K., Lindsley, D.H., 1983. Apollo 14 very low titanium glasses; melting experiments in iron-platinum alloy capsules. in: W.V. Boynton, G. Schubert, (Eds), 14th Lunar and Planetary Science Conference 88, American Geophysical Union, pp. 335-342.

Delano, J.W., 1986. Pristine lunar glasses; criteria, data, and implications. in: G. Ryder, G. Schubert, (Eds), Sixteenth lunar and planetary science conference 91, American Geophysical Union, pp. D201-D213.

Draper, D.S., du Frane, S.A., Dwarzski, R.E., Shearer, C.K., Agee, C.B., 2006. High-pressure phase equilibria and element partitioning experiments on Apollo 15 green C picritic glass: Implications for the role of garnet in the deep lunar interior. Geochimica et Cosmochimica Acta 70 2400-2416.

Edmunson, J.E., Borg, L.E., Nyquist, L.E., Asmerom, Y., 2009. A combined Sm/Nd, Rb/Sr, and U/Pb isotopic study of Mg-suite norite 78238; further evidence for early differentiation of the Moon. Geochimica et Cosmochimica Acta 73 514-527.

Elardo, S.M., Draper, D.S., Shearer, C.K., 2010. Magma Ocean Composition and the Lunar Mantle: Implications for the Source Lithologies of the Highlands Magnesian Suite. 41st Lunar and Planetary Science Conference Abstract #1450.

Elkins-Tanton, L.T., Chatterjee, N., Grove, T.L., 2003a. Experimental and petrological constraints on lunar differentiation from the Apollo 15 green picritic glasses. Meteoritics & Planetary Science 38 515-527.

Elkins-Tanton, L.T., Parmentier, E.M., Hess, P.C., 2003b. Magma ocean fractional crystallization and cumulate overturn in terrestrial planets: Implications for Mars. Meteoritics and Planetary Science 38 1753-1771.

Elkins-Tanton, L.T., Van Orman, J.A., Hager, B.H., Grove, T.L., 2002. Re-examination of the lunar magma ocean cumulate overturn hypothesis; melting or mixing is required. Earth and Planetary Science Letters 196 239-249.

Elkins, L.T., Fernandes, V.A., Delano, J.W., Grove, T.L., 2000. Origin of lunar ultramafic green glasses; constraints from phase equilibrium studies. Geochimica et Cosmochimica Acta 64 2339-2350.

Grove, T.L., Bryan, W.B., 1983. Fractionation of pyroxene-phyric MORB at low pressure; an experimental study. Contributions to Mineralogy and Petrology 84 293-309.

Hess, P.C., 1994. Petrogenesis of lunar troctolites. Journal of Geophysical Research 99 19,083-019,093.

Hess, P.C., Parmentier, E.M., 1995. A model for the thermal and chemical evolution of the Moon's interior; implications for the onset of mare volcanism. Earth and Planetary Science Letters 134 501-514.

Holloway, J.R., Pan, V., Gudmundsson, G., 1992. High-pressure fluid-absent melting experiments in the presence of graphite; oxygen fugacity, ferric/ferrous ratio and dissolved CO (sub 2). European Journal of Mineralogy 4 105-114.

Jones, J.H., 1984. Temperature- and pressure-independent correlations of olivine/liquid partition coefficients and their application to trace element partitioning. Contributions to Mineralogy and Petrology 88 126-132.

Kennedy, G.C., Higgins, G.H., 1975. A lunar core and the Moon's magnetic field. The Moon 12 401-406.

Kesson, S.E., Lindsley, D.H., 1976. Mare basalt petrogenesis; a review of experimental studies. Reviews of Geophysics and Space Physics 14 361-373.

Khan, A., Maclennan, J., Taylor, S.R., Connolly, J.A.D., 2006. Are the Earth and the Moon compositionally alike? Inferences on lunar composition and implications for lunar origin and evolution from geophysical modeling. Journal of Geophysical Research-Planets 111.

Li, J., Agee, C.B., 1996. Geochemistry of mantle-core differentiation at high pressure. Nature 381 686-689.

Longhi, J., 1980. A model of early lunar differentiation. Proceedings of the Lunar and Planetary Science Conference 289-315.

Longhi, J., 1992a. Experimental petrology and petrogenesis of mare volcanics. Geochimica et Cosmochimica Acta 56 2235-2251.

Longhi, J., 1992b. Origin of picritic green glass magmas by polybaric fractional fusion. Lunar and planetary science 22 343-353.

Longhi, J., 2003. A new view of lunar ferroan anorthosites; postmagma ocean petrogenesis. Journal of Geophysical Research 108 16.

Longhi, J., 2006. Petrogenesis of picritic mare magmas: Constraints on the extent of early lunar differentation. Geochimica et Cosmochimica Acta 70 5919-5934.

Longhi, J., Durand, S.R., Walker, D., 2010. The pattern of Ni and Co abundances in lunar olivines. Geochimica et Cosmochimica Acta 74 784-798.

McCallum, I.S., Schwartz, J.M., 2001. Lunar Mg suite; thermobarometry and petrogenesis of parental magmas. Journal of Geophysical Research 106 27,969-927,983.

McKay, G., Le, L., Schwandt, C., Mikouchi, T., Koizumi, E., Jones, J.H., 2004. Yamato 980459: The most primitive shergottite? 35th Lunar and Planetary Science Conference.

Miller, G.H., Stolper, E.M., Ahrens, T.J., 1991. The equation of state of a molten komatiite; 2, Application to komatiite petrogenesis and the Hadean mantle. Journal of Geophysical Research 96 11,849-811,864.

Neal, C.R., 2001. Interior of the Moon: The presence of garnet in the primitive deep lunar mantle. Journal of Geophysical Research 106 27865-27885.

Neal, C.R., Taylor, L.A., 1992. Petrogenesis of mare basalts; a record of lunar volcanism. Geochimica et Cosmochimica Acta 56 2177-2211.

Nyquist, L.E., Shih, C.Y., 1992. The isotopic record of lunar volcanism. Geochimica et Cosmochimica Acta 56 2213-2234.

Ohtani, E., 1985. The primordial terrestrial magma ocean and its implication for stratification of the mantle. Physics of the Earth and Planetary Interiors 38 70-80.

Papike, J.J., Ryder, G., Shearer, C.K., 1998. Lunar samples. Reviews in Mineralogy 36 5 1-5 234.

Pritchard, M.E., Stevenson, D.J., 2000. Thermal aspects of a lunar origin by giant impact. in: R.M. Canup, K. Righter, (Eds), Origin of the earth and moon The University of Arizona space science series, University of Arizona Press in collaboration with Lunar and Planetary Institute, Houston, Tucson, pp. 179-196.

Righter, K., Drake, M.J., 1997. A magma ocean on Vesta; core formation and petrogenesis of eucrites and diogenites. Meteoritics and Planetary Science 32 929-944.

Riner, M.A., Lucey, P.G., Desch, S.J., McCubbin, F.M., 2009. Nature of opaque components on Mercury: Insights into a Mercurian magma ocean. Geophysical Research Letters 36.

Roeder, P.L., Emslie, R.F., 1970. Olivine-liquid equilibrium. Contributions to Mineralogy and Petrology 29 275-289.

Ryder, G., Norman, M.D., Taylor, G.J., 1997. The complex stratigraphy of the highland crust in the Serenitatis region of the Moon inferred from mineral fragment chemistry. Geochimica et Cosmochimica Acta 61 1083-1105.

Schubert, G., 1979. Subsolidus convection in the mantles of terrestrial planets. Annual Review of Earth and Planetary Sciences 7 289-342.

Shearer, C.K., Hess, P.C., Wieczorek, M.A., Pritchard, M.E., Parmentier, E.M., Borg, L.E., Longhi, J., Elkins-Tanton, L.T., Neal, C.R., Antonenko, I., Canup, R.M., Halliday, A.N., Grove, T.L., Hager, B.H., Lee, D.C., Wiechert, U., Jolliff, B.L., 2006a. Thermal and magmatic evolution of the Moon. Reviews in Mineralogy and Geochemistry 60 365-518.

Shearer, C.K., McKay, G., Papike, J.J., Karner, J.M., Shearer, C., Vaniman, D., Labotka, T., 2006b. Valence state partitioning of vanadium between olivine-liquid; estimates of the oxygen fugacity of Y980459 and application to other olivine-phyric Martian basalts. American Mineralogist 91 1657-1663.

Shearer, C.K., Papike, J.J., 1993. Basaltic magmatism on the Moon; a perspective from volcanic picritic glass beads. Geochimica et Cosmochimica Acta 57 4785-4812.

Shearer, C.K., Papike, J.J., 1999. Magmatic evolution of the Moon. American Mineralogist 84 1469-1494.

Shearer, C.K., Papike, J.J., 2005. Early crustal building processes on the Moon; models for the petrogenesis of the magnesian suite. Geochimica et Cosmochimica Acta 69 3445-3461.

Shih, C.Y., Nyquist, L.E., Dasch, E.J., Bogard, D.D., Bansal, B.M., Wiesmann, H., 1993. Ages of pristine noritic clasts from lunar breccias 15445 and 15455. Geochimica et Cosmochimica Acta 57 915-931.

Smith, J.V., Anderson, A.T., Newton, R.C., Olsen, E.J., Wyllie, P.J., 1970. A petrologic model for the Moon based on petrogenesis, experimental petrology, and physical properties. Journal of Geology 78 381-405.

Snyder, G.A., Borg, L.E., Nyquist, L.E., Taylor, L.A., 2000. Chronology and isotopic constraints on lunar evolution. in: R.M. Canup, K. Righter, (Eds), Origin of the Earth and Moon, University of Arizona Press, pp. 361-395.

Snyder, G.A., Taylor, L.A., Neal, C.R., 1992. A chemical model for generating the sources of mare basalts; combined equilibrium and fractional crystallization of the lunar magmasphere. Geochimica et Cosmochimica Acta 56 3809-3823.

Spera, F.J., 1992. Lunar magma transport phenomena. Geochimica et Cosmochimica Acta 56 2253-2256.

Stolper, E., 1980. Predictions of mineral assemblages in planetary interiors. Proceedings of the Lunar and Planetary Science Conference 235-250.

Taylor, S.R., 1982. Planetary science; a lunar perspective. Lunar and Planetary Institute, Houston, TX, 481 pp.

Taylor, S.R., Jakeš, P., 1974. The geochemical evolution of the Moon. Proceedings of the 5th Lunar Science Conference 1287-1305.

Taylor, S.R., Taylor, G.J., Taylor, L.A., 2006. The Moon: A Taylor perspective. Geochimica et Cosmochimica Acta 70 5904-5918.

Tonks, W.B., Melosh, H.J., 1990. The physics of crystal settling and suspension in a turbulent magma ocean, Origin of the Earth, Oxford Univ. Press, New York, NY, United States (USA), pp. 151-174.

Tonks, W.B., Melosh, H.J., 1993. Magma ocean formation due to giant impacts. Journal of Geophysical Research 98 5319-5333.

Ulmer, P., 1989. The dependence of the Fe2+-Mg cation-partitioning between olivine and basaltic liquid on pressure, temperature and composition; an experimental study to 30 kbars. Contributions to Mineralogy and Petrology 101 261-273.

Warren, P.H., 1985. The magma ocean concept and lunar evolution. Annual Review of Earth and Planetary Sciences 13 201-240.

Warren, P.H., Wasson, J.T., 1979. Origin of KREEP. Reviews of Geophysics and Space Physics 17 73-88.

Wieczorek, M.A., Jolliff, B.L., Khan, A., Pritchard, M.E., Weiss, B.P., Williams, J.G., Hood, L.L., Righter, K., Neal, C.R., Shearer, C.K., McCallum, I.S., Tompkins, S., Hawke, B.R., Peterson, C., Gillis, J.J., Bussey, B., 2006. The constitution and structure of the lunar interior. Reviews in Mineralogy and Geochemistry 60 221-364.

Wood, J.A., Dickey, J.S., Jr., Marvin, U.B., Powell, B.N., 1970. Lunar anorthosites and a geophysical model of the Moon. Proceedings of the Apollo 11 Lunar Science Conference 965-988.

7. TABLES AND FIGURES

	TWM (Taylor 1982)	LPUM Longhi (2006)	TWM This Study	LPUM This Study
SiO_2	44.4	46.1	44.3	45.9
TiO_2	0.31	0.17	0.31	0.15
Al_2O_3	6.10	3.90	6.45	4.15
FeO	10.90	7.60	10.62	8.15
MnO	0.15	0.13	0.15	0.12
MgO	32.70	38.30	32.83	38.40
CaO	4.60	3.20	4.69	2.95
Na_2O	0.09	0.05	0.24	0.10
K_2O	0.01	0.01	0.01	0.01
P_2O_5	0.01	0.01	0.01	0.01
Cr_2O_3	0.61	0.50	0.61	0.50
Ni	-	-	0.025	0.025
Co	-	-	0.025	0.025
Y	-	-	0.025	0.025
V	-	-	0.025	0.025
Mg*	84	90	84.6	89.4
CaO/ Al_2O_3	0.75	0.82	0.73	0.71

Table 1: The Taylor Whole Moon (TWM) and Lunar Primitive Upper Mantle (LPUM) bulk silicate Moon compositions of Taylor (1982) and Longhi (2006) with the compositions used in this study. The TWM represents a 50% enrichment in refractory elements relative to bulk Earth while the LPUM has no such enrichment. Ni, Co, Y and V were added to the bulk compositions used in this study in the arbitrary value of 250 ppm to investigate their partitioning behavior. All values except Mg* and CaO/ Al_2O_3 are in Wt. %.

Run #	TWM 2.008	TWM 2.006	TWM 2.014	TWM 2.020	TWM 2.015	TWM 2.003	TWM 2.004	TWM 2.010	TWM 2.021	TWM 2.007	TWM 2.023	TWM 2.011	TWM 2.022	TWM 2.013
Pressure (GPa)	1	1	1	1	1	2	2	2	2	2	4	4	4	4
Temp (°C)	1550	1450	1350	1300	1250	1700	1600	1500	1450	1400	1825	1800	1775	1750
Duration (mins)	120	120	150	240	210	150	120	120	272	120	60	60	90	120
Modal Abundances	74% li 26% ol	56% li 44% ol	50% li 50% ol <1% sp	45% li 55% ol <1% sp	32% li 48% ol 17% opx 3% sp	97% li 3% ol	71% li 29% ol	59% li 41% ol	50% li 44% ol 6% opx	33% li 42% ol 24% opx	74% li 26% ol	50% li 32% ol 9% opx 9% gt	35% li 27% ol 23% opx 15% gt	31% li 35% ol 17% opx 17% gt
Sum R^2	0.433	0.258	0.130	0.260	1.769	0.177	0.030	0.281	0.018	0.206	0.867	0.075	0.016	0.193
Olivine Comp (Fo)	92.0	90.1	89.6	88.9	90.2	93.8	91.6	90.2	89.4	89.3	92.1	90.7	89.3	89.6
Olivine K_D	0.32	0.33	0.31	0.31	0.22	0.33	0.34	0.34	0.33	0.26	0.35	0.31	0.32	0.33
OPX Comp (En, Fs, Wo)	-	-	-	-	$En_{82}Fs_{13}Wo_5$	-	-	-	$En_{87}Fs_{10}Wo_3$	$En_{82}Fs_{14}Wo_4$	-	$En_{89}Fs_8Wo_3$	$En_{87}Fs_9Wo_4$	$En_{86}Fs_{10}Wo_4$
Spinel Comp (Hy, Ch, Sp)	-	-	$Hy_{35}Ch_{38}Sp_{27}$	$Hy_{36}Ch_{37}Sp_{27}$	$Hy_{45}Ch_{29}Sp_{26}$	-	-	-	-	-	-	-	-	-
Garnet Comp (Py, Alm, Gr)	-	-	-	-	-	-	-	-	-	-	-	$Py_{81}Al_{11}Gr_8$	$Py_{79}Al_{13}Gr_{11}$	$Py_{76}Al_{13}Gr_{11}$
Melt Mg*	79.3	75.6	73.5	71.7	67.5	84	79.5	76.3	74.3	69.8	80.7	75.6	73.5	74.3
Melt CaO/Al_2O_3	0.73	0.72	0.75	0.76	0.82	0.7	0.7	0.74	0.77	0.94	0.62	0.99	1.57	1.49
Ol D_{Ni} (EPMA)	2.2	3.0	5.6	3.4	5.0	2.2	2.5	3.3	4.1	4.4	2.3	5.2	2.6	2.6
Ol D_{Co} (EPMA)	0.9	1.1	1.4	1.8	1.2	0.8	1.2	1.2	1.5	1.0	1.0	0.8	1.1	0.8
Ol D_V (SIMS)	0.143	nd	nd	nd	nd	0.112	nd	nd	nd	nd	0.128	nd	nd	nd
Ol D_Y (SIMS)	0.008	nd	nd	nd	nd	0.008	nd	nd	nd	nd	0.005	nd	nd	nd
OPX D_Y (EPMA)	-	-	-	-	0.08	-	-	-	bdl	0.04	-	bdl	bdl	bdl
Gt D_Y (EPMA)	-	-	-	-	-	-	-	-	-	-	-	2.79	2.98	3.17
Sp D_V (EPMA)	-	-	2.02	10.77	8.77	-	-	-	-	-	-	-	-	-

Table 2: Taylor Whole Moon equilibrium crystallization experimental results.
nd = No Data, bdl = Below detection limit, - = Not applicable, Li = Liquid, Ol = Olivine, OPX = Low-Ca pyroxene, Gt = Garnet, Sp = spinel. D_X = Concentration of element X in mineral/concentration of element X in melt

Run #	LPUM 2.011	LPUM 2.002	LPUM 2.016	LPUM 2.003	LPUM 2.014	LPUM 2.009	LPUM 2.010	LPUM 2.012	LPUM 2.007	LPUM 2.006	LPUM 2.015	LPUM 2.005	LPUM 2.008	LPUM 2.017	LPUM 2.018
Pressure (GPa)	1	1	1	1	1	1	1	2	2	2	2	2	2	4	4
Temp (°C)	1700	1600	1500	1450	1400	1350	1250	1750	1700	1600	1550	1500	1400	1800	1750
Duration (mins)	60	60	60	90	235	180	240	60	60	60	240	150	180	60	90
Modal Abundances	76% Li 24% Ol	58% Li 42% Ol	50% Li 50% Ol	45% Li 55% Ol	41% Li 59% Ol	30% Li 57% Ol 13% OPX	21% Li 56% Ol 23% OPX	76% Li 24% Ol	70% Li 30% Ol	55% Li 45% Ol	49% Li 51% Ol	33% Li 48% Ol 19% OPX	20% Li 48% Ol 32% OPX	48% Li 34% Ol 18% OPX	31% Li 41% Ol 25% OPX 3% Gt
Sum R^2	0.380	0.194	0.444	0.183	0.494	0.143	1.075	0.473	0.029	0.257	0.094	0.051	0.985	0.024	0.069
Ol Comp (Fo)	95.6	94.1	93.1	92.3	91.6	91.3	92.7	95.0	94.4	93.1	92.6	91.8	92.4	93.2	92.0
Olivine K_D	0.31	0.29	0.30	0.35	0.34	0.31	0.22	0.34	0.35	0.36	0.35	0.33	0.31	0.35	0.33
OPX Comp (En, Fs, Wo)	-	-	-	-	-	$En_{89}Fs_9$ Wo_2	$En_{85}Fs_{11}$ Wo_4	-	-	-	-	$En_{90}F_8$ Wo_2	$En_{86}Fs_{11}$ Wo_3	$En_{92}Fs_6$ Wo_2	$En_{90}Fs_7$ Wo_3
Gt Comp (Py, Alm, Gr)	-	-	-	-	-	-	-	-	-	-	-	-	-	-	$Py_{82}Al_{10}$ Gr_8
Melt Mg*	87.2	82.7	80.1	81.0	78.8	76.9	74.3	86.8	86.0	83.0	81.6	78.9	79.4	82.9	79.6
Melt CaO/Al_2O_3	0.76	0.70	0.80	0.79	0.82	0.82	0.85	0.71	0.70	0.81	0.75	0.80	1.10	0.72	0.94
Ol D_{Ni} (EPMA)	2.4	2.4	3.7	2.5	1.3	5.2	3.4	3.9	3.5	3.0	5.9	4.2	3.6	2.5	2.5
Ol D_{Co} (EPMA)	0.5	1.0	1.0	1.2	1.5	1.6	1.8	0.8	0.8	1.1	1.4	1.1	1.3	0.9	0.9
Ol D_V (SIMS)	nd	nd	nd	nd	nd	nd	nd	nd	nd	nd	nd	nd	nd	nd	nd
Ol D_Y (SIMS)	nd	nd	nd	nd	nd	nd	nd	nd	nd	nd	nd	nd	nd	nd	nd
OPX D_Y EPMA)	-	-	-	-	-	bdl	0.02	-	-	-	-	bdl	bdl	0.03	bdl
Gt D_Y (EPMA)	-	-	-	-	-	-	-	-	-	-	-	-	-	-	3.3

Table 3: Lunar Primitive Upper Mantle equilibrium crystallization experimental results.
nd = No Data, bdl = Below detection limit, - = Not applicable, Li = Liquid, Ol = Olivine, OPX = Low-Ca pyroxene, Gt = Garnet
D_X = Concentration of element X in mineral/concentration of element X in melt

	TWM Cumulate Pile (50% Solid)	LPUM Cumulate Pile (50% Solid)	GGSa (Longhi, 2006)	GGSp (Longhi, 2006)	TWM Residual LMO	LPUM Residual LMO
SiO_2	41.73	42.40	44.2	52.1	46.94	49.39
TiO_2	0.03	0.01	0.08	0.19	0.61	0.30
Al_2O_3	1.69	0.57	1.21	2.47	11.55	7.94
FeO	9.41	6.84	16.2	12.1	11.62	10.09
MnO	0.12	0.09	0.18	0.14	0.18	0.17
MgO	45.87	50.46	36.4	29.4	18.85	24.93
CaO	0.65	0.38	1.27	2.29	9.14	6.10
Na_2O	0.01	0.01	0.03	0.13	0.38	0.27
K_2O	0.003	0.02	0.002	0.005	0.02	0.03
Cr_2O_3	0.65	0.31	0.43	1.31	0.53	0.62
Mg*	89.7	92.9	80.0	81.2	74.3	81.5
CaO/Al_2O_3	0.39	0.67	1.05	0.93	0.79	0.77

Table 4: Compositions of the TWM and LPUM cumulate piles containing 3% trapped instantaneous residual liquid, with the olivine-dominated green glass source region (GGSa) and low-Ca pyroxene-dominated green glass source region (GGSp) from Longhi (2006) and the compositions of the residual magma oceans after removal the 50% cumulates. All values except Mg* and CaO/Al_2O_3 in wt. % oxide

Normative Mineral	TWM Residual 25% Solid	LPUM Residual 25% Solid	TWM Residual 50% Solid	LPUM Residual 50% Solid	TWM Residual 70% Solid	LPUM Residual 70% Solid
Plagioclase	25.60	15.15	32.97	22.65	40.04	30.11
Orthoclase	0.12	0.06	0.12	0.18	0.18	0.24
Diopside	6.13	4.41	12.46	7.80	17.57	12.86
Hypersthene	23.24	33.83	29.47	46.44	17.08	38.07
Olivine	42.74	45.20	22.72	21.14	22.89	16.74
Ilmenite	0.82	0.38	1.16	0.57	1.52	0.87
Apatite	0.05	0.02	0.05	0.05	0.07	0.09
Chromite	1.52	1.10	1.13	1.34	0.59	1.05

Table 5: Results of CIPW norm calculations for the weighted residual LMO compositions after ~25, 50 and 70% equilibrium crystallization. All values in normative wt. %.

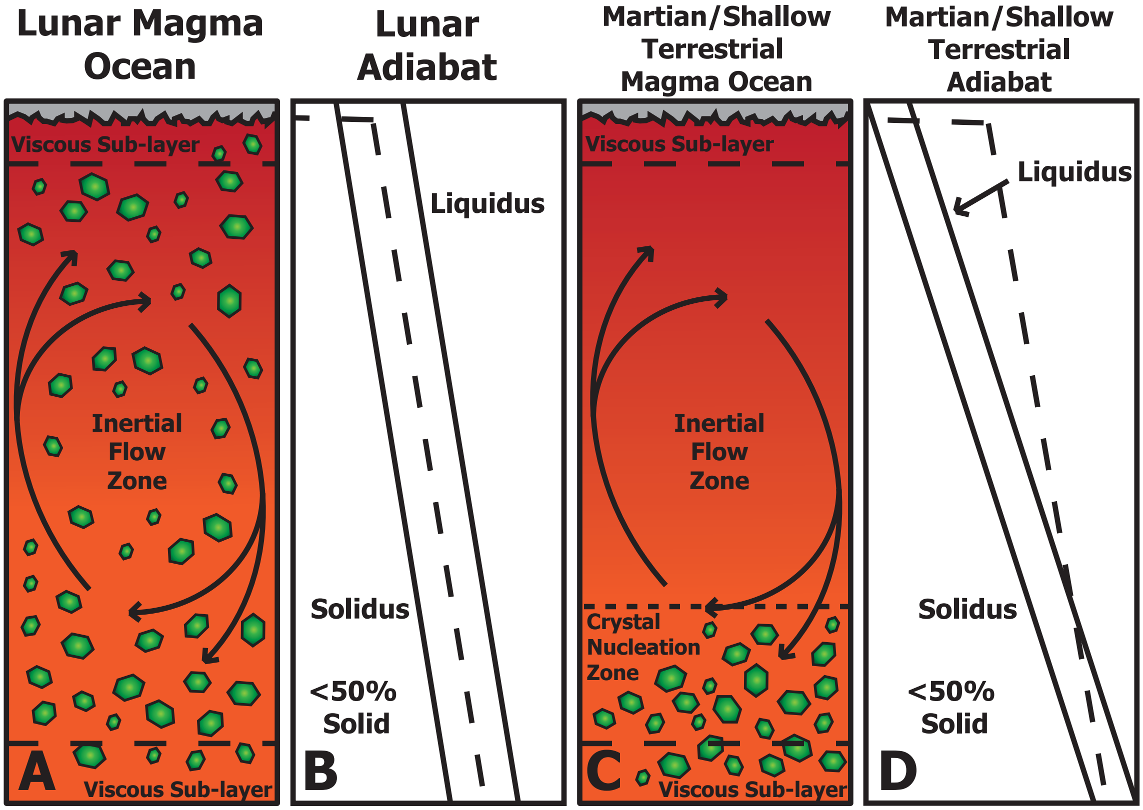

Figure 1: (A) A crystallizing and turbulently convecting Lunar Magma Ocean at <50% solid. Crystals can nucleate at all depths and will not dissolve when carried to shallower/deeper depths in the column. (B) The adiabat assumed here for a Lunar Magma Ocean lies between the solidus and liquidus at all depths, allowing crystallization throughout the column. (C) A Martian or shallow terrestrial turbulently convecting magma ocean at <50% solid. Crystallization can occur only in the crystal nucleation zone, the region where the adiabat is between the solidus and liquidus. Crystals swept into the region above, where the adiabat is above the liquidus, will dissolve. (D) A possible adiabat for a Martian or shallow terrestrial magma ocean. The slopes (dT/dz) of the liquidus and solidus are higher than for the Moon due to the greater acceleration of gravity, causing the adiabat in this model to be above the liquidus at shallow depths and cross it deeper in the column, initiating crystallization below that depth.

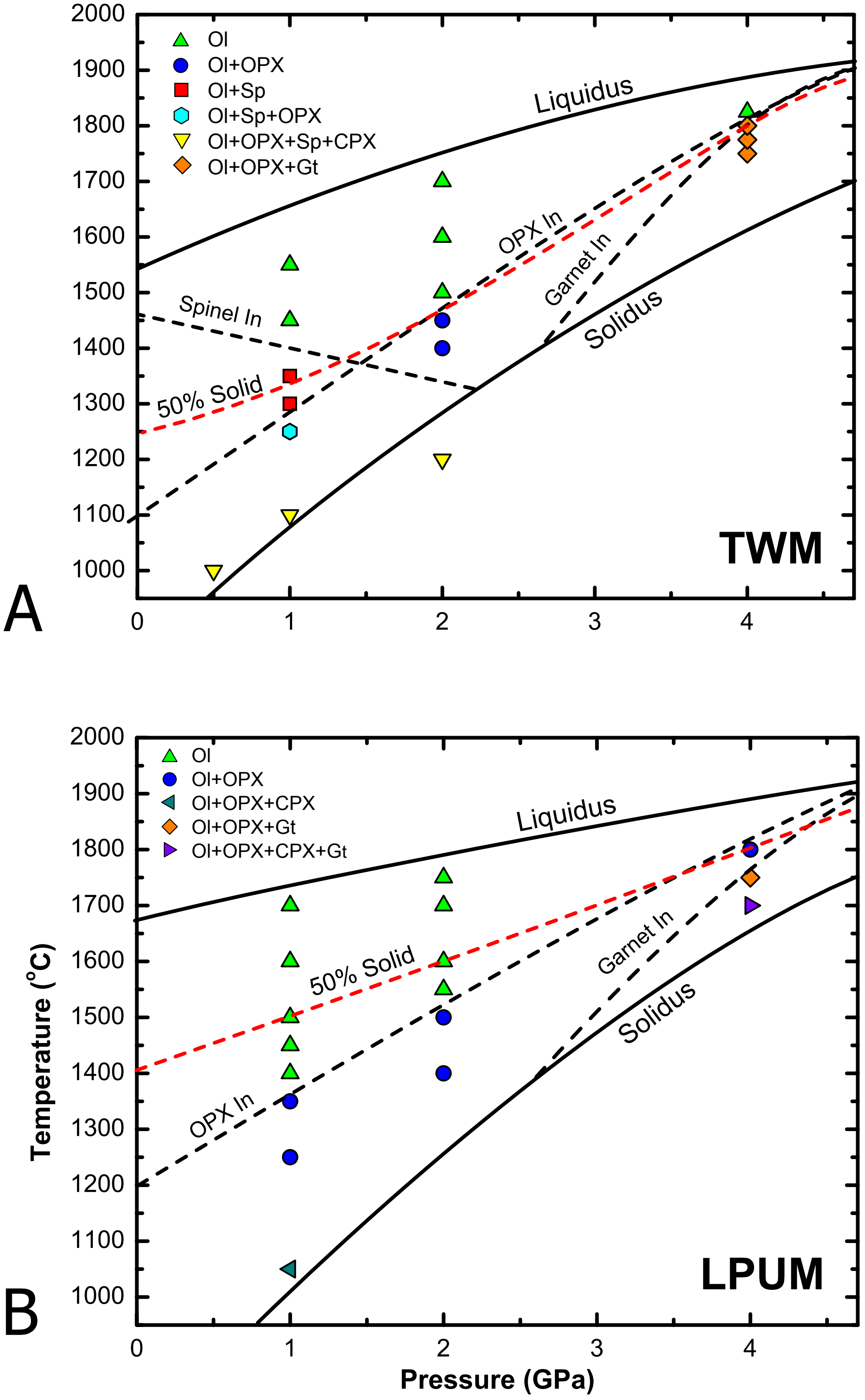

Figure 2: Experimental temperature vs. pressure phase diagrams for (A) the Taylor Whole Moon composition and (B) the Lunar Primitive Upper Mantle composition with approximate liquidus, solidus, mineral-in curves and 50% solid curves for each.

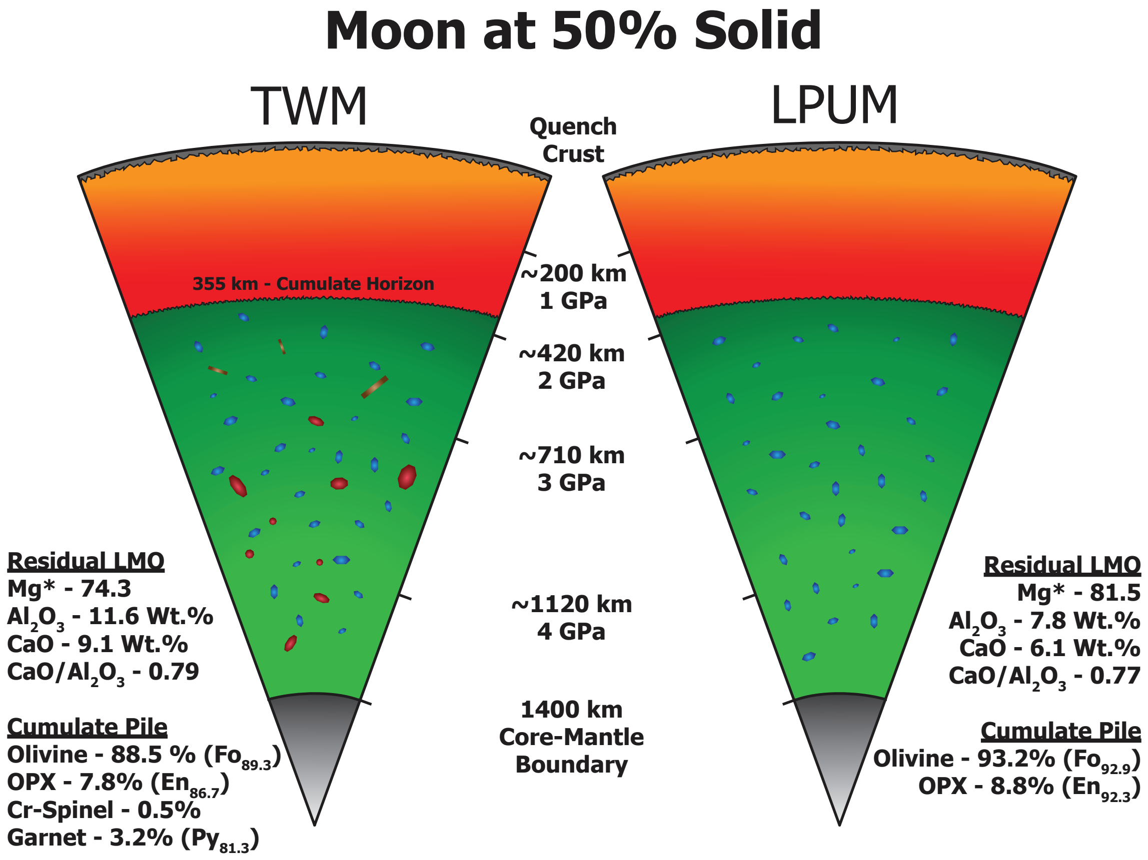

Figure 3: The composition of the residual LMO and cumulate pile for the TWM and LPUM bulk Moon compositions at 50% solid, after convection has waned, suspended crystals have settled, and fractional crystallization of the residual liquid begins. Model assumes an initally completly molten Moon and a core radius of 337 km.

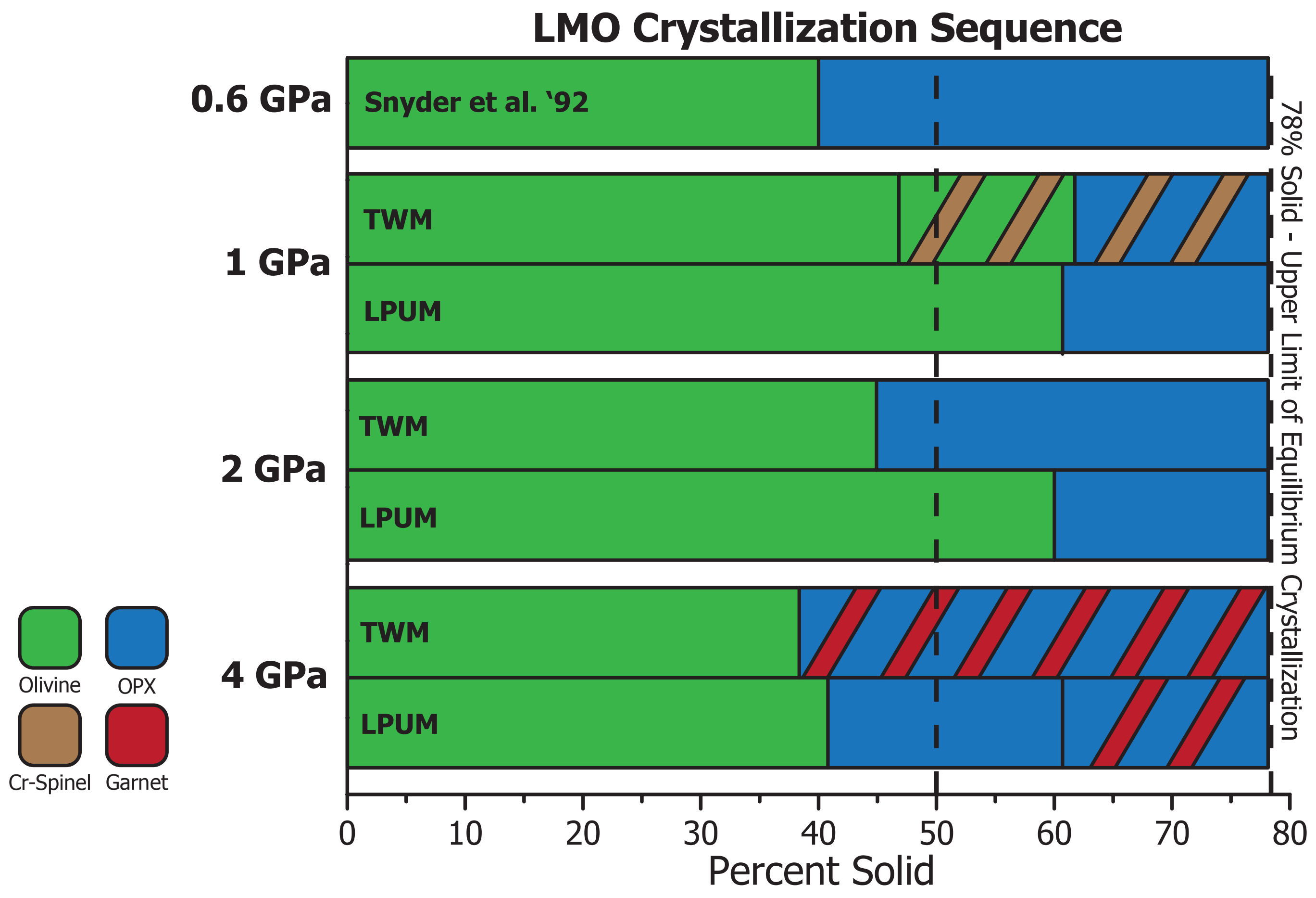

Figure 4: Comparison of the Taylor Whole Moon and Lunar Primitive Upper Mantle equilibrium crystallization sequences at 1, 2 and 4 GPa with the LMO crystallization sequence from the model of Snyder et al. (1992) at 0.6 GPa. 50% solid represents the end of equilibrium crystallization in this work. 78% solid represents the end of equilibrium crystallization in the Snyder et al. model and this value is taken as an absolute upper limit.

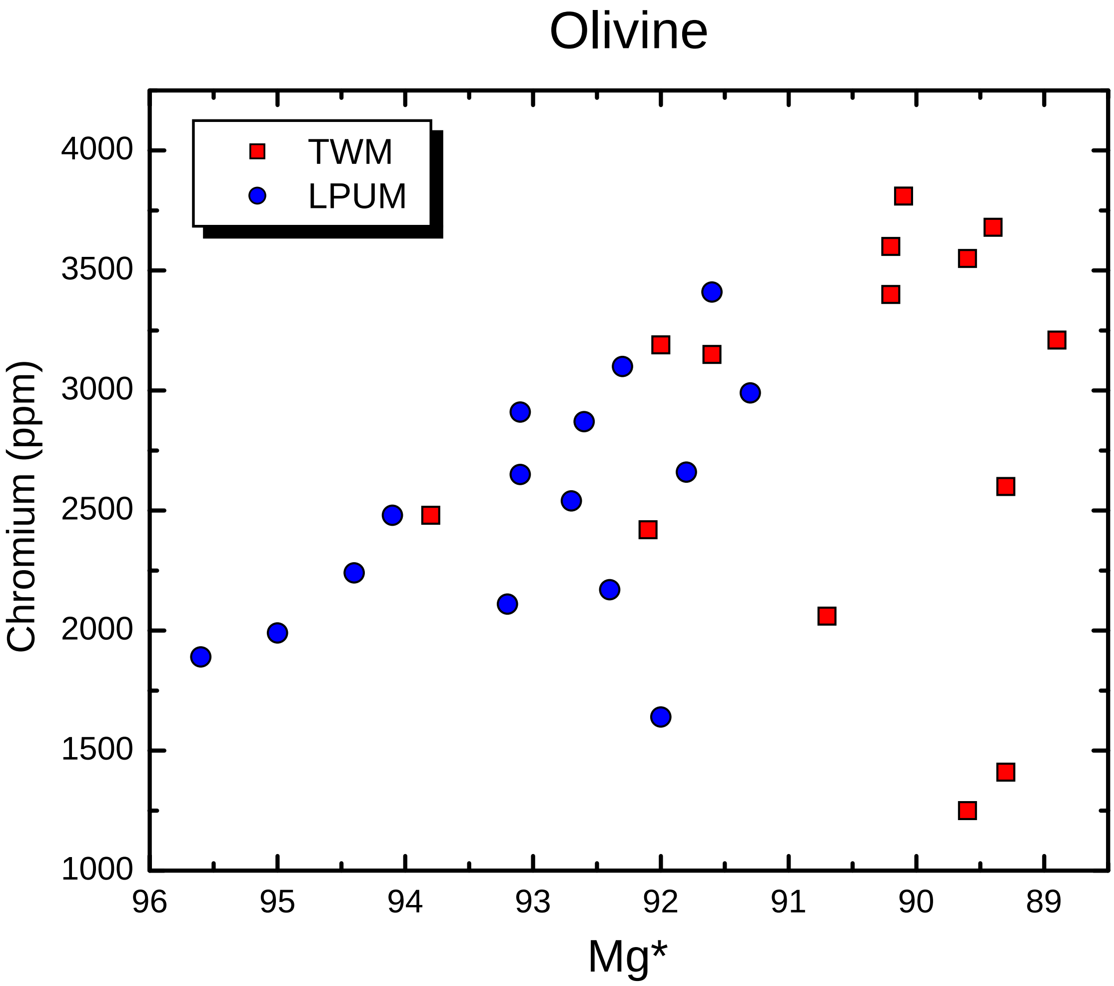

Figure 5: The Cr content in parts per million of olivine produced by equilibrium crystallization as a function of olivine Mg* for both the TWM and LPUM bulk Moon compositions.

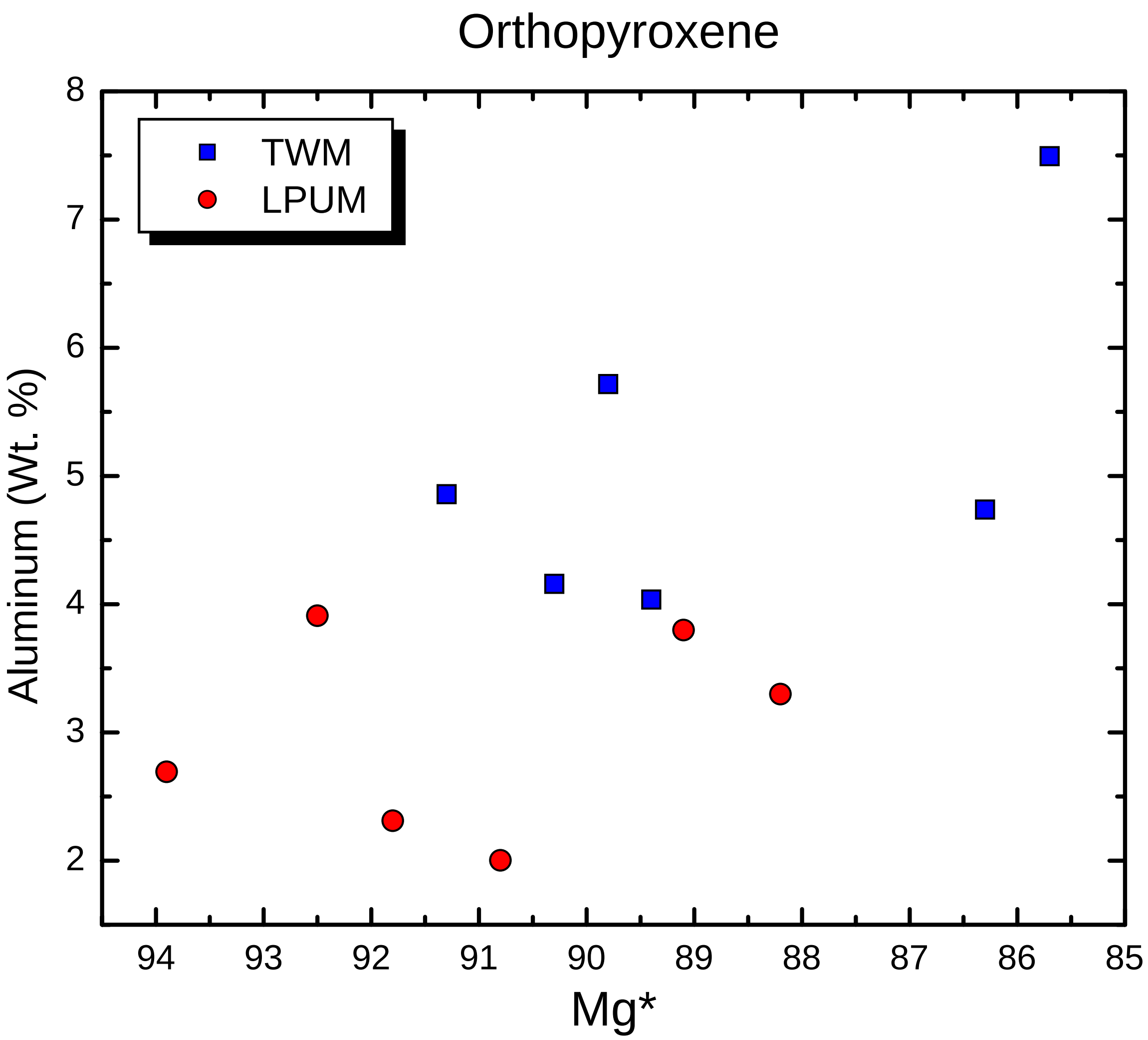

Figure 6: The Al content in wt. % of OPX produced by equilibrium crystallization of the TWM and LPUM bulk Moon compositions.

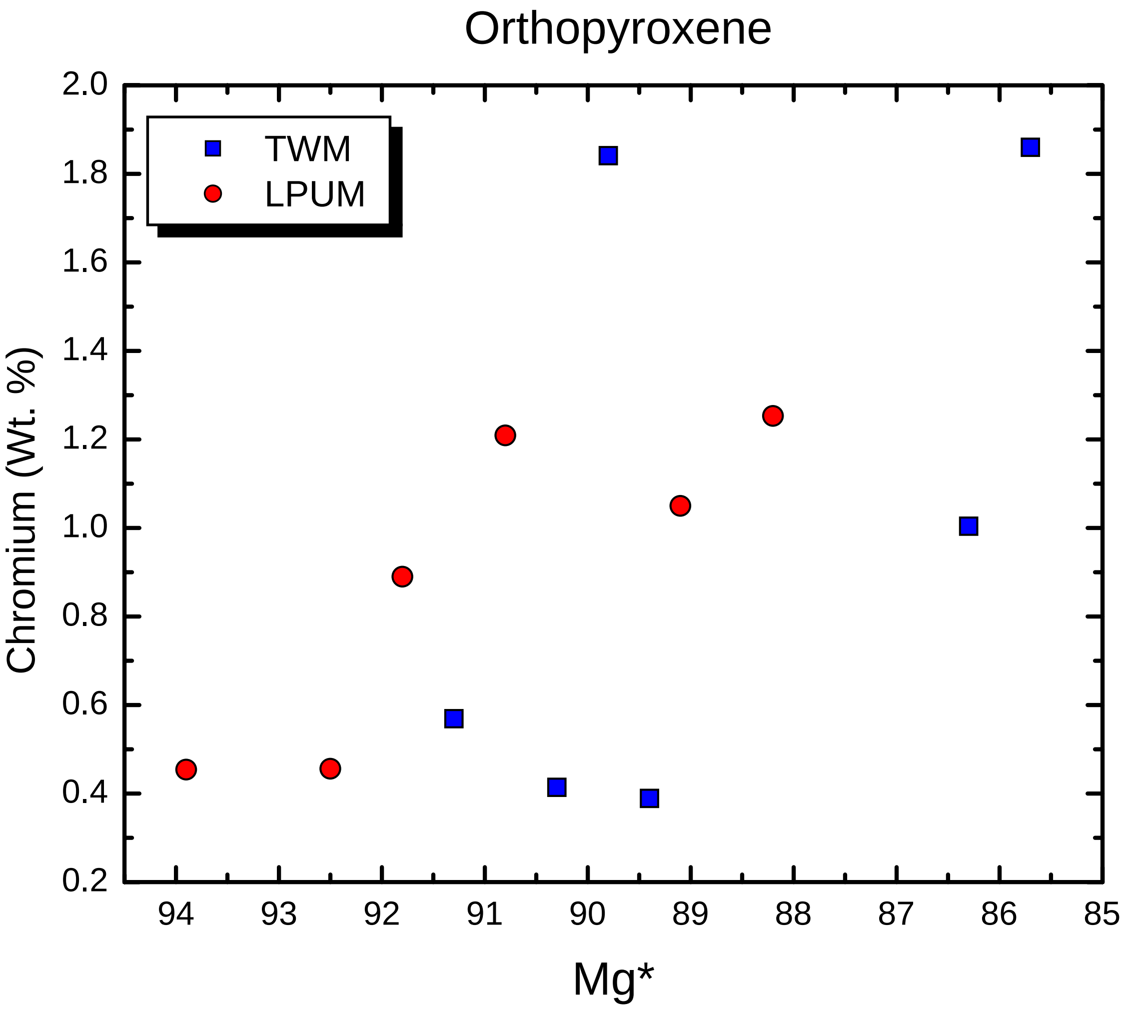

Figure 7: The Cr content in wt. % of OPX produced by equilibrium crystallization of the TWM and LPUM bulk Moon compositions.

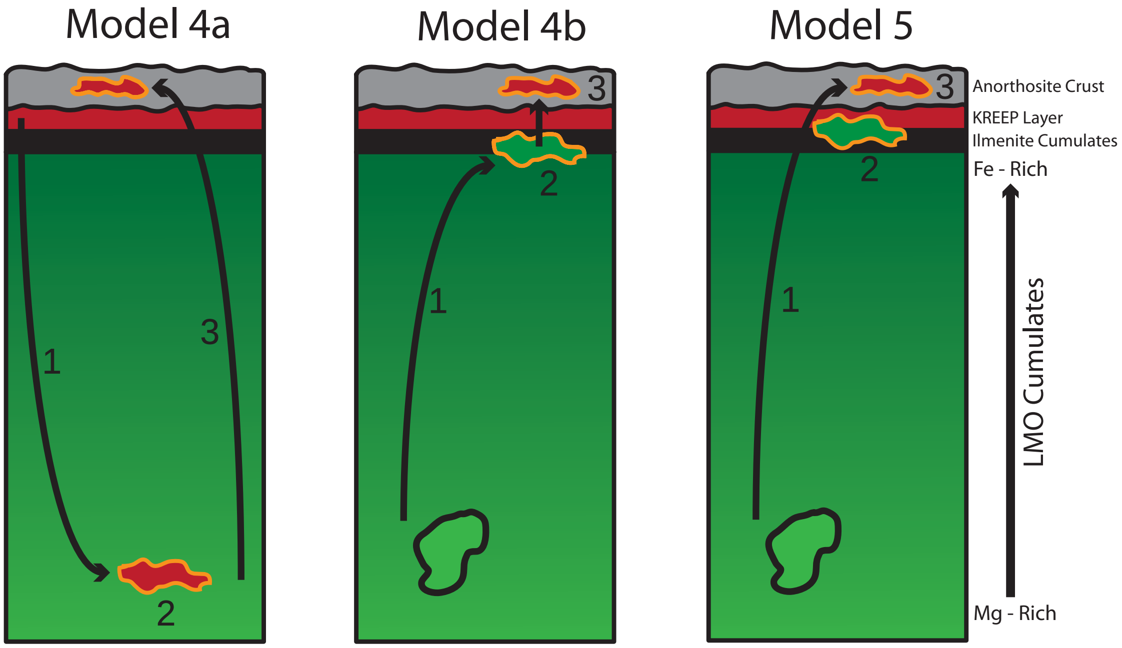

Model 4a

1. Cumulate overturn hybridizes deep mantle with KREEP
2. Heat produced by KREEP partially melts early cumulates
3. High Mg*, KREEP-rich melts rise and are emplaced in crust to form Mg-suite

Model 4b

1. Cumulate overturn brings hot, bouyant, high-Mg* cumulates to shallow depths
2. KREEP hybridizes overturned Mg-rich LMO cumulates
3. KREEP-rich partial melts intrude the crust and form the Mg-suite

Model 5

1. Cumulate overturn brings hot, bouyant, high-Mg* cumulates to shallow depths
2. Decompression partially melts the early cumulates
3. Partial melts assimilate KREEP and are emplaced in crust to form Mg-suite

Figure 8: Models for the formation of the Mg-suite.

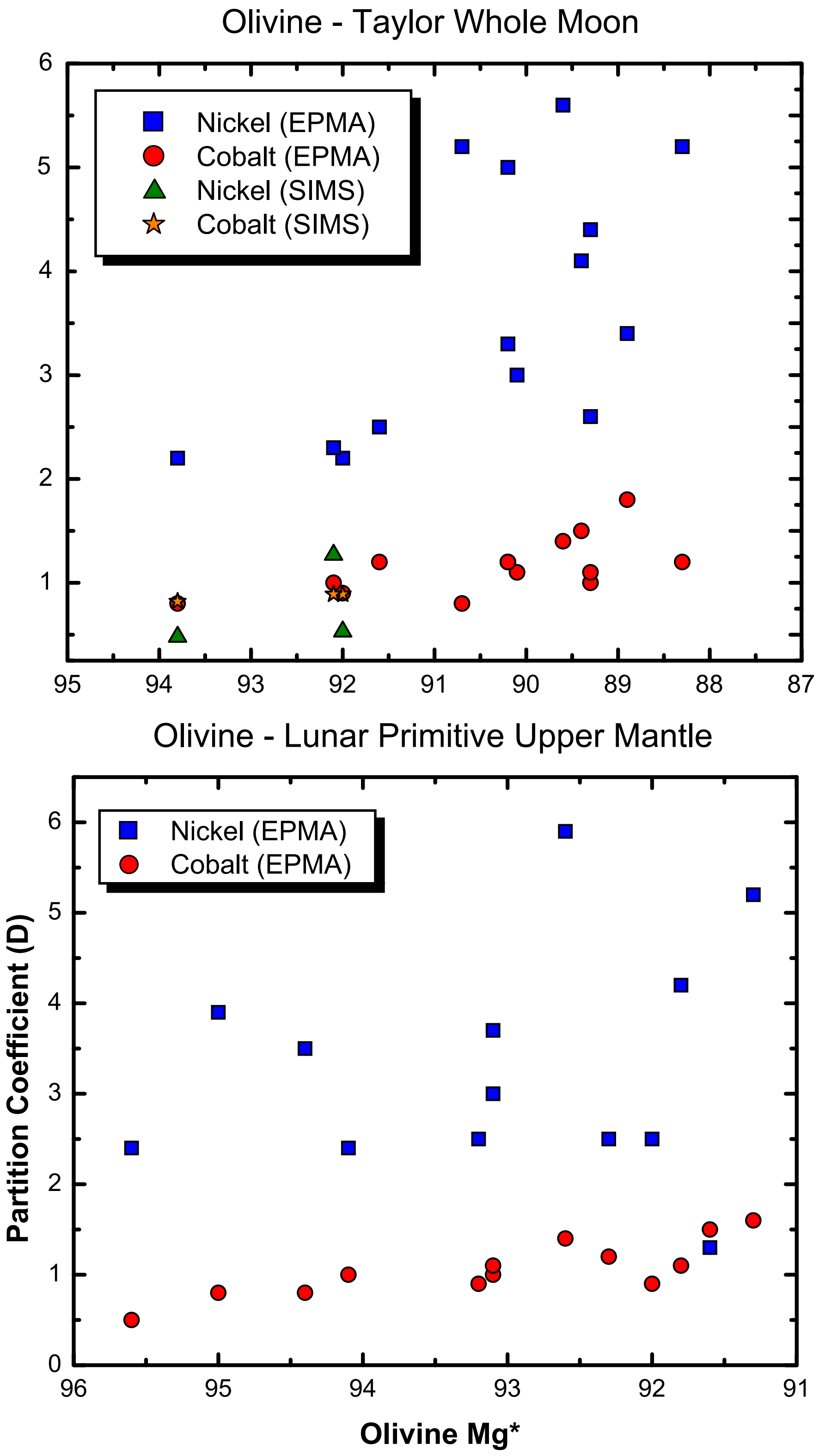

Figure 9: Partition coefficients of Ni and Co in olivine as a function of olivine Mg* for the Taylor Whole Moon and Lunar Primitive Upper Mantle bulk Moon Compositions.

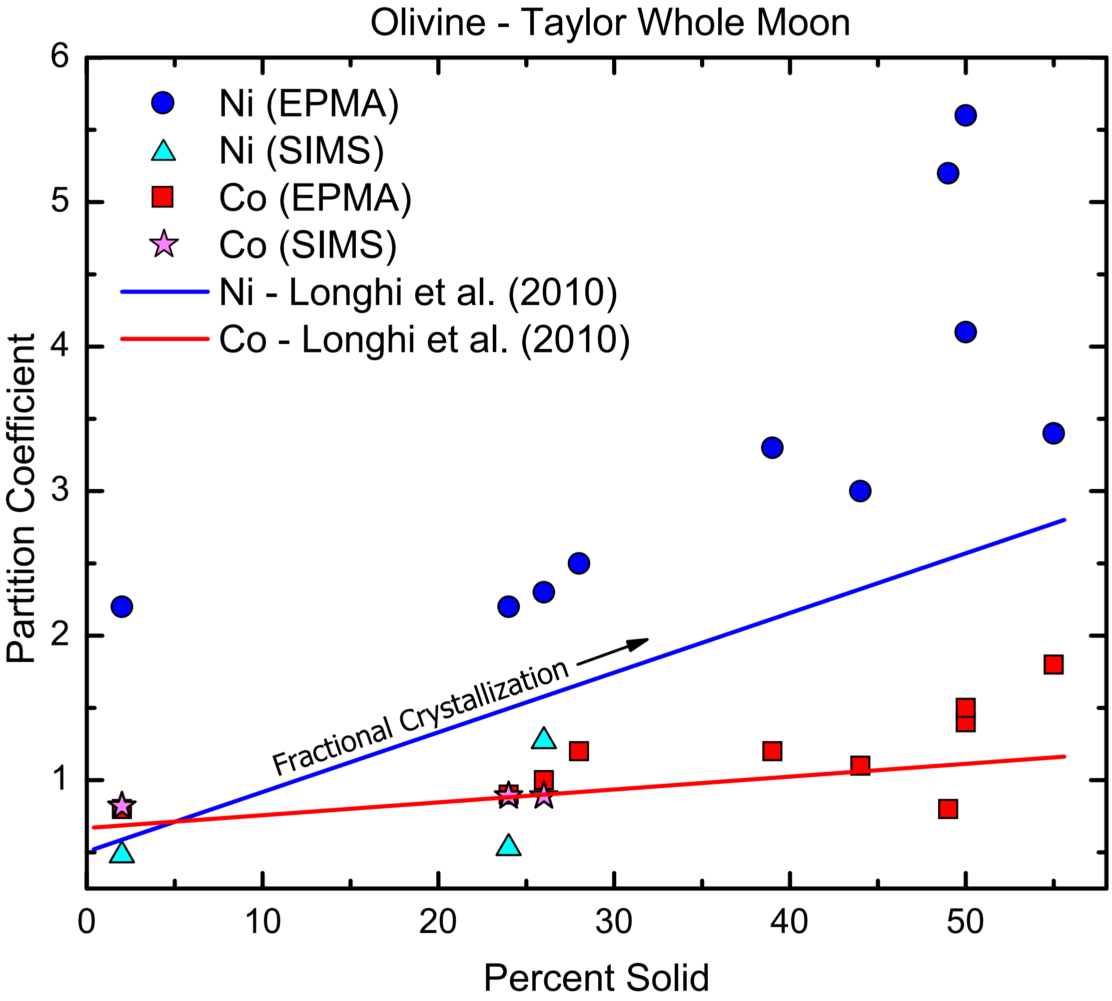

Figure 10: Plot of partition coefficients for Ni and Co in olivine from the Taylor Whole Moon equilibrium crystallization experiments as a function of percent solid. Solid lines are trends from Longhi et al. (2010) for a fractionally crystallizing LMO. The Longhi et al. data, the EPMA and SIMS data for Co, and the SIMS data for Ni all suggest early partition coefficients below unity (1) that increase as crystallization proceeds and olivine becomes more Fe-rich.

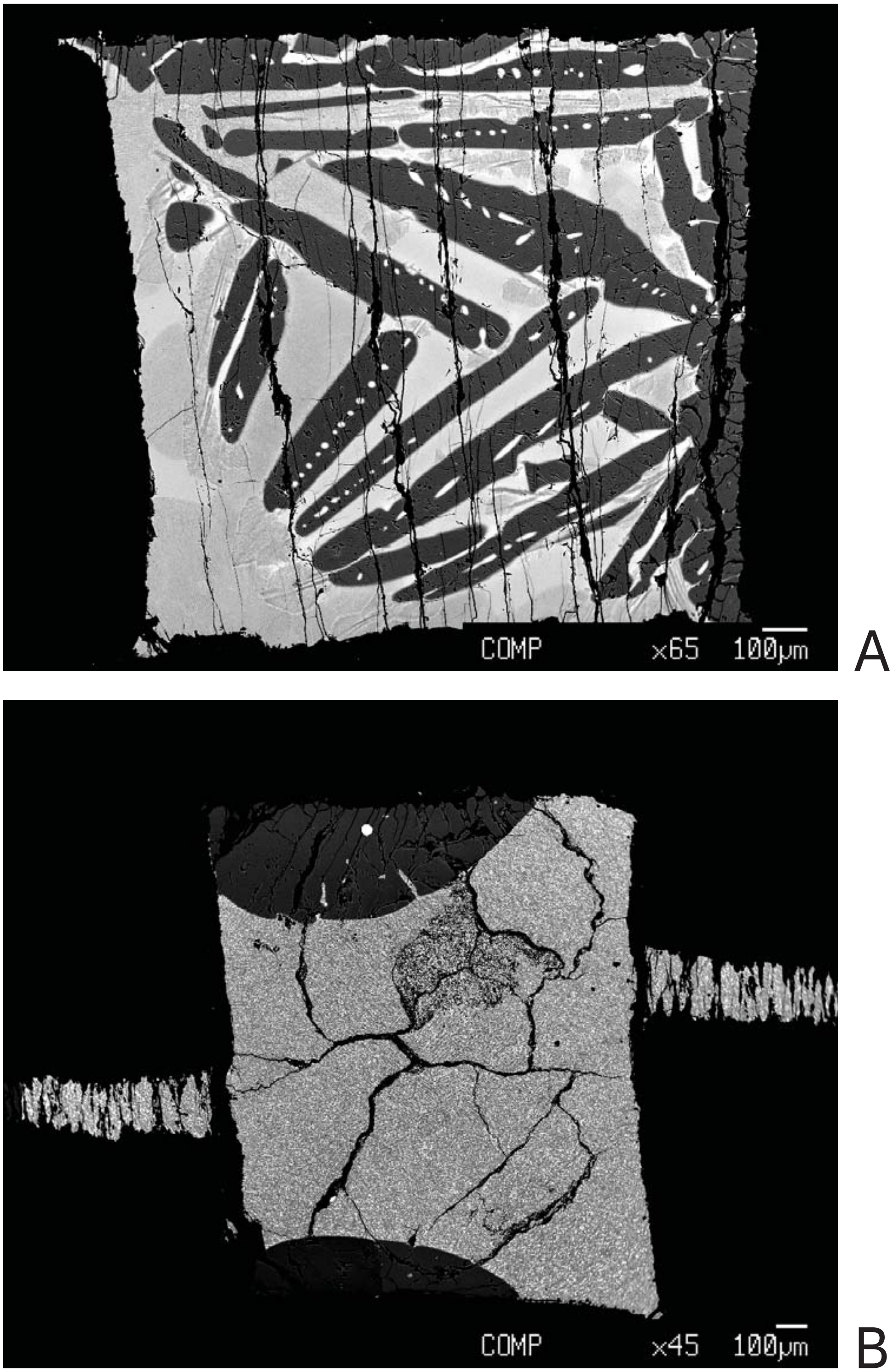

Appendix A: Back scattered electron images of typical experimental run products. (A) LPUM 2.015, conducted in a Depths of the Earth QUICKPress at 2 GPa, 1550 degrees C. Dark blades are olivine crystals and bright patches are quenched melt. The graphite capsule appears black. (B) TWM 2.013, conducted in a Walker-style multianvil press at 4 GPa, 1750 degrees C was an unsuccessful run, but is sufficient to show the crystal morphology typical of multianvil run products.

	TWM 2.003		TWM 2.004		TWM 2.006		TWM 2.007			TWM 2.008
	Quench	Olivine	Quench	Olivine	Quench	Olivine	Quench	Olivine	OPX	Quench
SiO_2	44.009	41.896	44.906	41.611	46.180	41.308	43.113	40.200	51.655	44.331
TiO_2	0.324	0.007	0.430	0.006	0.548	0.012	0.867	0.012	0.104	0.424
Al_2O_3	6.901	0.165	9.128	0.172	11.310	0.140	13.445	0.164	7.494	8.490
FeO	10.926	5.888	11.608	8.028	11.525	9.304	11.366	10.083	8.493	12.206
MnO	0.155	0.071	0.175	0.099	0.179	0.111	0.172	0.114	0.144	0.175
MgO	32.258	52.204	25.207	50.875	20.037	48.736	14.730	49.353	28.627	26.226
CaO	4.826	0.178	6.372	0.187	8.135	0.221	12.589	0.223	1.987	6.224
Na_2O	0.202	0.003	0.257	0.001	0.423	0.003	0.504	0.002	0.030	0.328
K_2O	0.012	0.002	0.019	0.001	0.022	0.001	0.035	0.001	0.002	0.021
P_2O_5	0.010	0.004	0.013	0.003	0.018	0.005	0.039	0.002	0.004	0.023
Cr_2O_3	0.609	0.248	0.715	0.315	0.734	0.381	0.218	0.260	1.860	0.707
NiO	0.004	0.009	0.006	0.015	0.007	0.021	0.013	0.058	0.012	0.006
CoO	0.039	0.032	0.034	0.039	0.033	0.037	0.035	0.036	0.025	0.038
Y_2O_3	0.021	0.002	0.034	0.000	0.049	0.003	0.099	0.005	0.004	0.034
V_2O_3	0.018	0.000	0.033	0.000	0.059	0.002	0.067	0.000	0.027	0.042
Total	100.314	100.707	98.938	101.353	99.258	100.285	97.292	100.513	100.467	99.275

Appendix B: Electron microprobe analyses for all experiments on the Taylor Whole Moon bulk Moon composition presented here. All values in wt. % oxide.

	TWM 2.010		TWM 2.014			TWM 2.015				TWM 2.016	
Olivine	Quench	Olivine	Quench	Olivine	Spinel	Quench	Olivine	OPX	Spinel	Quench	Olivine
40.785	45.128	40.324	47.684	40.767	0.386	47.381	41.060	54.109	0.581	48.730	41.573
0.011	0.520	0.009	0.6255	0.008	0.298	0.889	0.006	0.127	0.358	1.068	0.014
0.123	10.495	0.167	12.649	0.143	26.325	15.830	0.134	4.738	34.107	19.058	0.153
7.588	11.395	9.233	10.6466	9.890	12.558	9.418	9.418	8.409	13.989	9.799	7.092
0.087	0.170	0.107	0.1787	0.125	0.284	0.165	0.120	0.168	0.241	0.142	0.091
50.785	20.594	49.031	16.547	49.144	16.016	10.984	49.869	29.650	15.736	6.012	51.896
0.209	7.809	0.191	9.4939	0.220	0.146	12.982	0.212	2.490	0.242	10.879	0.214
0.006	0.317	0.003	0.4659	0.000	0.000	0.616	0.001	0.011	0.000	1.561	0.001
0.001	0.027	0.000	0.0288	0.002	0.002	0.038	0.002	0.001	0.000	0.103	0.001
0.002	0.029	0.005	0.0248	0.003	0.002	0.037	0.004	0.005	0.001	0.096	0.003
0.319	0.729	0.360	0.5217	0.355	42.783	0.143	0.340	1.004	33.093	0.037	0.316
0.012	0.017	0.057	0.0062	0.035	0.015	0.006	0.030	0.009	0.023	0.009	0.032
0.034	0.038	0.045	0.0376	0.053	0.059	0.035	0.040	0.026	0.060	0.027	0.031
0.004	0.041	0.000	0.0586	0.005	0.006	0.096	0.002	0.007	0.000	0.121	0.003
0.001	0.048	0.000	0.0571	0.000	0.115	0.061	0.002	0.050	0.533	0.045	0.000
99.969	97.355	99.531	99.0254	100.749	98.993	98.679	101.240	100.804	98.964	97.687	101.420

			TWM 2.019				TWM 2.018				
OPX	CPX	Spinel	Olivine	OPX	CPX	Spinel	Quench	Olivine	OPX	CPX	Spinel
52.034	49.204	0.670	40.506	50.174	48.461	0.486	55.228	41.451	48.771	45.849	0.785
0.285	0.548	0.649	0.014	0.264	0.485	0.275	0.537	0.012	0.523	1.071	1.145
6.391	8.906	29.858	0.222	8.102	7.068	39.015	20.442	0.124	7.571	11.550	25.403
12.030	11.617	19.549	8.410	10.771	8.329	18.464	6.002	6.559	13.447	11.149	21.157
0.191	0.233	0.288	0.108	0.171	0.174	0.224	0.072	0.075	0.225	0.246	0.317
26.372	17.553	12.665	50.151	26.229	19.089	14.552	3.434	51.921	23.318	12.006	11.019
2.665	10.973	0.227	0.214	2.547	14.750	0.173	10.180	0.210	6.011	17.004	0.245
0.045	0.148	0.000	0.002	0.070	0.363	0.004	1.609	0.001	0.037	0.070	0.003
0.004	0.008	0.002	0.001	0.002	0.004	0.005	0.099	0.000	0.002	0.002	0.001
0.006	0.011	0.002	0.007	0.004	0.008	0.008	0.063	0.005	0.004	0.018	0.003
0.285	0.742	35.753	0.357	0.663	0.367	26.655	0.027	0.321	0.285	0.383	38.071
0.015	0.009	0.017	0.058	0.016	0.016	0.028	0.007	0.015	0.007	0.004	0.008
0.047	0.034	0.082	0.039	0.030	0.025	0.071	0.016	0.030	0.033	0.035	0.076
0.014	0.059	0.006	0.000	0.007	0.069	0.001	0.055	0.003	0.044	0.136	0.009
0.021	0.094	0.609	0.000	0.033	0.034	0.271	0.008	0.000	0.021	0.088	0.874
100.403	100.140	100.391	100.088	99.082	99.243	100.232	97.779	100.727	100.298	99.611	99.073

TWM 2.020			TWM 2.021			TWM 2.022				TWM 2.023
Quench	Olivine	Spinel	Quench	Olivine	OPX	Quench	Olivine	OPX	Garnet	Quench
48.417	40.552	0.239	45.616	40.556	53.019	40.138	38.462	52.983	41.736	44.126
0.715	0.010	0.401	0.604	0.003	0.060	0.634	0.006	0.021	0.214	0.399
13.974	0.154	26.786	11.714	0.165	5.717	6.068	0.204	4.159	21.169	9.508
9.577	10.600	13.130	11.266	10.059	6.330	14.545	10.156	6.089	6.516	11.235
0.165	0.130	0.270	0.178	0.113	0.117	0.188	0.109	0.097	0.152	0.163
13.589	48.693	16.264	18.279	49.055	31.174	22.644	48.926	31.979	23.487	26.325
10.650	0.218	0.150	9.036	0.191	1.354	9.537	0.235	1.994	3.868	5.881
0.474	0.001	0.000	0.350	0.003	0.015	0.265	0.010	0.063	0.001	0.165
0.030	0.001	0.002	0.019	0.003	0.001	0.028	0.002	0.002	0.001	0.013
0.028	0.002	0.003	0.025	0.002	0.005	0.037	0.004	0.000	0.006	0.010
0.321	0.321	41.226	0.644	0.368	1.841	0.234	0.141	0.414	1.699	0.650
0.011	0.036	0.013	0.013	0.049	0.023	0.016	0.041	0.019	0.012	0.017
0.025	0.044	0.062	0.030	0.047	0.013	0.051	0.054	0.030	0.021	0.036
0.081	0.003	0.002	0.061	0.001	0.000	0.029	0.001	0.000	0.085	0.023
0.052	0.000	0.564	0.037	0.000	0.020	0.070	0.005	0.010	0.062	0.054
98.110	100.765	99.110	97.874	100.615	99.689	94.483	98.355	97.860	99.030	98.602

	TWM 2.011				TWM 2.013			
Olivine	Quench	Olivine	OPX	Garnet	Quench	Olivine	OPX	Garnet
41.414	44.251	41.285	55.609	43.818	42.762	40.656	55.446	43.019
0.003	0.519	0.006	0.026	0.166	0.756	0.003	0.032	0.247
0.321	7.974	0.274	4.858	21.880	6.560	0.222	4.036	21.774
7.564	13.603	8.835	5.502	5.900	14.910	11.045	6.629	6.989
0.083	0.192	0.100	0.088	0.138	0.195	0.117	0.102	0.170
50.894	23.672	49.885	32.480	24.015	21.425	48.182	31.422	22.379
0.170	7.875	0.188	1.479	3.069	10.089	0.245	2.197	4.374
0.006	0.221	0.003	0.039	0.004	0.295	0.006	0.066	0.001
0.001	0.021	0.001	0.000	0.002	0.027	0.001	0.002	0.004
0.003	0.023	0.002	0.000	0.006	0.037	0.007	0.005	0.005
0.242	0.325	0.206	0.569	1.934	0.229	0.125	0.389	1.618
0.038	0.009	0.046	0.013	0.005	0.008	0.040	0.014	0.008
0.036	0.048	0.039	0.027	0.021	0.039	0.049	0.026	0.024
0.002	0.026	0.002	0.000	0.073	0.030	0.001	0.000	0.094
0.004	0.064	0.003	0.003	0.043	0.071	0.003	0.011	0.052
100.780	98.823	100.875	100.693	101.075	97.432	100.703	100.377	100.758

	LPUM 2.002		LPUM 2.003		LPUM 2.006		LPUM 2.007		LPUM 2.005		
	Quench	Olivine	Quench	Olivine	Quench	Olivine	Quench	Olivine	Quench	Olivine	OPX
SiO_2	48.018	41.614	51.163	40.783	49.118	41.480	47.473	40.800	46.589	40.029	55.478
TiO_2	0.250	0.009	0.334	0.005	0.283	0.006	0.213	0.006	0.443	0.003	0.024
Al_2O_3	7.033	0.078	8.208	0.060	6.652	0.097	6.030	0.096	10.239	0.149	2.311
FeO	10.398	5.705	9.312	7.398	9.764	6.677	9.243	5.469	10.064	7.876	5.422
MnO	0.164	0.082	0.154	0.091	0.156	0.082	0.153	0.072	0.171	0.100	0.100
MgO	27.912	52.824	22.223	51.103	27.055	51.895	31.774	52.957	21.145	50.769	33.909
CaO	4.936	0.142	6.488	0.142	5.353	0.130	4.192	0.131	8.140	0.164	0.917
Na_2O	0.307	0.002	0.356	0.002	0.220	0.000	0.178	0.001	0.321	0.001	0.002
K_2O	0.017	0.001	0.030	0.003	0.021	0.002	0.020	0.002	0.037	0.002	0.002
P_2O_5	0.007	0.003	0.020	0.003	0.013	0.006	0.015	0.002	0.034	0.002	0.005
Cr_2O_3	0.603	0.248	0.608	0.310	0.589	0.265	0.538	0.224	0.511	0.266	0.890
NiO	0.009	0.021	0.011	0.026	0.021	0.062	0.010	0.035	0.008	0.036	0.018
CoO	0.035	0.033	0.034	0.040	0.039	0.043	0.043	0.035	0.038	0.043	0.023
Y_2O_3	0.034	0.003	0.057	0.000	0.034	0.004	0.027	0.003	0.086	0.001	0.000
V_2O_3	0.023	0.000	0.041	0.000	0.026	0.000	0.010	0.000	0.050	0.000	0.007
Total	99.745	100.766	99.037	99.965	99.343	100.748	99.916	99.831	97.876	99.441	99.109

Appendix C: Electron microprobe analyses for all experiments on the Lunar Primitive Upper Mantle bulk Moon composition presented here. All values in wt. % oxide.

LPUM 2.008			LPUM 2.009			LPUM 2.010			LPUM 2.011		LPUM 2.012
Quench	Olivine	OPX	Quench	Olivine	OPX	Quench	Olivine	OPX	Quench	Olivine	Quench
46.147	40.064	53.588	50.740	40.494	55.455	49.204	41.491	55.079	47.616	41.945	46.821
0.715	0.013	0.054	0.511	0.008	0.046	0.692	0.005	0.097	0.204	0.011	0.197
12.600	0.101	3.798	11.834	0.069	2.002	15.073	0.072	3.299	5.202	0.065	5.396
7.751	7.305	6.916	8.681	8.347	6.040	7.343	7.103	7.433	8.698	4.231	9.117
0.153	0.092	0.127	0.157	0.115	0.125	0.131	0.082	0.148	0.134	0.054	0.141
16.953	51.332	31.604	16.240	50.524	33.333	11.918	51.778	31.060	33.723	53.597	33.583
13.809	0.169	1.608	9.721	0.171	1.203	12.852	0.152	2.212	3.967	0.127	3.812
0.212	0.001	0.019	0.422	0.001	0.004	0.738	0.004	0.007	0.230	0.001	0.135
0.005	0.002	0.001	0.037	0.002	0.002	0.052	0.001	0.001	0.013	0.002	0.013
0.030	0.004	0.002	0.044	0.006	0.004	0.062	0.007	0.003	0.012	0.007	0.015
0.317	0.217	1.050	0.481	0.299	1.209	0.237	0.254	1.253	0.497	0.189	0.523
0.015	0.055	0.018	0.004	0.023	0.005	0.005	0.018	0.013	0.006	0.013	0.003
0.028	0.037	0.033	0.031	0.050	0.026	0.021	0.039	0.035	0.038	0.020	0.033
0.174	0.004	0.000	0.107	0.001	0.000	0.158	0.002	0.003	0.026	0.001	0.024
0.081	0.001	0.023	0.047	0.000	0.016	0.031	0.000	0.023	0.011	0.000	0.018
98.989	99.395	98.841	99.057	100.110	99.469	98.518	101.007	100.665	100.376	100.263	99.829

	LPUM 2.014		LPUM 2.015		LPUM 2.018				LPUM 2.016	
Olivine	Quench	Olivine	Quench	Olivine	Quench	Olivine	OPX	Garnet	Quench	Olivine
41.984	51.195	41.221	49.755	41.163	44.355	40.325	54.701	43.014	48.610	39.715
0.002	0.394	0.011	0.302	0.001	0.357	0.010	0.016	0.154	0.295	0.007
0.098	9.307	0.063	8.031	0.090	7.472	0.219	3.910	21.410	7.660	0.111
4.876	9.273	8.143	9.435	7.226	11.778	7.663	4.841	5.521	9.998	6.657
0.059	0.169	0.104	0.165	0.087	0.185	0.089	0.083	0.138	0.162	0.088
52.815	19.404	50.795	23.599	51.552	25.714	50.728	33.278	24.196	23.303	51.810
0.124	7.645	0.161	6.006	0.128	6.999	0.174	1.376	3.352	6.178	0.145
0.001	0.453	0.000	0.282	0.002	0.224	0.004	0.039	0.003	0.304	0.003
0.002	0.028	0.002	0.029	0.001	0.049	0.003	0.002	0.003	0.023	0.002
0.001	0.032	0.002	0.017	0.003	0.043	0.007	0.007	0.010	0.020	0.001
0.199	0.594	0.341	0.614	0.287	0.400	0.164	0.456	1.864	0.609	0.291
0.011	0.009	0.011	0.007	0.041	0.015	0.038	0.018	0.002	0.005	0.017
0.027	0.030	0.047	0.035	0.048	0.048	0.043	0.022	0.009	0.039	0.040
0.000	0.068	0.001	0.041	0.006	0.043	0.000	0.000	0.140	0.062	0.000
0.000	0.026	0.000	0.032	0.000	0.057	0.000	0.005	0.058	0.041	0.001
100.197	98.628	100.899	98.350	100.635	97.736	99.468	98.751	99.874	97.306	98.886

LPUM 2.019					LPUM 2.017		
Quench	Olivine	OPX	CPX	Garnet	Quench	Olivine	OPX
40.016	39.395	54.438	42.872	42.113	44.527	39.041	53.995
0.740	0.007	0.028	0.681	0.224	0.277	0.005	0.013
4.420	0.135	2.356	4.188	20.757	7.447	0.209	2.693
14.025	9.557	6.479	14.913	6.942	10.211	6.553	4.028
0.203	0.107	0.112	0.184	0.172	0.162	0.078	0.070
23.701	49.838	32.268	26.927	22.721	27.855	51.705	34.880
10.291	0.216	2.585	8.563	4.516	5.348	0.133	0.899
0.262	0.001	0.082	0.245	0.004	0.160	0.003	0.019
0.028	0.001	0.001	0.006	0.003	0.029	0.002	0.001
0.070	0.003	0.009	0.044	0.004	0.036	0.003	0.000
0.337	0.120	0.325	0.303	2.022	0.594	0.211	0.454
0.015	0.036	0.016	0.024	0.007	0.013	0.032	0.014
0.055	0.051	0.022	0.060	0.019	0.042	0.039	0.022
0.090	0.001	0.000	0.046	0.144	0.048	0.000	0.001
0.104	0.001	0.002	0.112	0.084	0.047	0.006	0.008
94.358	99.470	98.724	99.167	99.732	96.796	98.020	97.097

	Ni (Cts/Sec)	Co (Cts/Sec)	Y (Cts/Sec)	V (Cts/Sec)	SiO_2 (Wt. %)
TWM 2.003					
Quench 1	82.915	188.389	532.897	208.096	
Quench 2	77.597	184.393	502.240	200.991	
Olivine 1	35.464	149.726	4.302	21.824	
Olivine 2	41.735	155.584	4.488	23.886	
Average Quench	80.256	186.391	517.568	204.544	44.01
Average Olivine	38.600	152.655	4.395	22.855	41.90
Olivine-Melt D	0.481	0.819	0.008	0.112	
TWM 2.008					
Quench 1	95.000	221.617	589.788	240.850	
Quench 2	104.927	219.575	627.250	248.312	
Olivine 1	56.400	198.254	5.029	35.219	
Olivine 2	48.696	194.490	5.019	34.543	
Average Quench	99.963	220.596	608.519	244.581	44.33
Average Olivine	52.548	196.372	5.024	34.881	40.79
Olivine-Melt D	0.526	0.890	0.008	0.143	
TWM 2.023					
Quench 1	381.329	227.984	538.069	212.491	
Quench 2	360.577	224.144	519.448	215.208	
Olivine 1	484.857	205.025	2.638	27.775	
Olivine 2	459.520	198.132	2.643	26.774	
Average Quench	370.953	226.064	528.758	213.850	44.13
Average Olivine	472.188	201.579	2.641	27.274	41.41
Olivine-Melt D	1.273	0.892	0.005	0.128	

Appendix D: SIMS data and calculated olivine/melt partition coefficients for experimental run products analyzed in this study.